

UNIVERSIDADE TECNOLÓGICA FEDERAL DO PARANÁ
PROGRAMA DE PÓS GRADUAÇÃO EM ENGENHARIA ELÉTRICA E
INFORMÁTICA INDUSTRIAL

JEAN PAULO NAKATU LONGO

SENSORS FOR HYDRATES DETECTION BASED ON
ELECTRICAL IMPEDANCE SPECTROSCOPY

DOCTORAL THESIS

CURITIBA

2020

JEAN PAULO NAKATU LONGO

**SENSORS FOR HYDRATES DETECTION BASED ON
ELECTRICAL IMPEDANCE SPECTROSCOPY**

Doctoral thesis presented to the Graduate Program in Electrical and Computer Engineering (CPGEI) of Federal University of Technology – Paraná (UTFPR), in partial fulfilment of the requirements for the degree of Doctor in Science (D.Sc.).

Advisor: Prof. Dr. Marco José da Silva.

Co-advisor: Prof. Dr. Rigoberto E.M. Morales

CURITIBA

2020

Dados Internacionais de Catalogação na Publicação

Longo, Jean Paulo Nakatu

Sensors for hydrates detection based on electrical impedance spectroscopy [recurso eletrônico] / Jean Paulo Nakatu Longo. -- 2020.

1 arquivo eletrônico (110 f.): PDF; 4,00 MB.

Modo de acesso: World Wide Web.

Texto em inglês com resumo em português.

Tese (Doutorado) - Universidade Tecnológica Federal do Paraná. Programa de Pós-graduação em Engenharia Elétrica e Informática Industrial. Área de Concentração: Engenharia de Automação e Sistemas. Linha de Pesquisa: Sistemas de Medição e Instrumentação, Curitiba, 2020.

Bibliografia: f. 95-107.

1. Engenharia elétrica - Teses. 2. Hidratos - Monitorização. 3. Oleodutos de petróleo. 4. Tubulação - Dinâmica dos fluidos. 5. Espectroscopia de impedância. 6. Detectores - Desenvolvimento. 7. Impedância (Eletricidade) - Medição. 8. Escoamento multifásico. 9. Garantia de fluxo (Engenharia do petróleo). 10. Métodos de simulação. I. Silva, Marco José da, orient. II. Melgarejo Morales, Rigoberto Eleazar, coorient. III. Universidade Tecnológica Federal do Paraná. Programa de Pós-graduação em Engenharia Elétrica e Informática Industrial. IV. Título.

CDD: Ed. 23 -- 621.3

Biblioteca Central do Câmpus Curitiba - UTFPR
Bibliotecária: Luiza Aquemi Matsumoto CRB-9/794

TERMO DE APROVAÇÃO DE TESE

A Tese de Doutorado intitulada **Sensors For Hydrates Detection Based On Electrical Impedance Spectroscopy**, defendida em sessão pública pelo(a) candidato(a) **Jean Paulo Nakatu Longo**, no dia **13 de março de 2020**, foi julgada aprovada em sua forma final para obtenção do título de Doutor em Ciências, Área de Concentração – **Engenharia de Automação e Sistemas**, Linha de Pesquisa – **Sistemas de Medição e Instrumentação**, pelo Programa de Pós-Graduação em Engenharia Elétrica e Informática Industrial.

BANCA EXAMINADORA:

Prof. Dr. Marco José da Silva – UTFPR - Orientador
Prof. Dr. Jean Carlos C. da Silva – UTFPR
Prof. Dr. Flavio Neves Junior – UTFPR
Prof. Dr. Amadeu Kun Wan Sum – CSM
Prof. Dr. Fernando Rangel de Souza – UFSC

A via original deste documento encontra-se arquivada na Secretaria do Programa, contendo a assinatura da Coordenação após a entrega da versão corrigida do trabalho.

Curitiba, 13 de março de 2020.

Carimbo e Assinatura do(a) Coordenador(a) do Programa

Acknowledgments

I thank my advisor Dr. Marco José da Silva for every effort and time devoted to me and to this work, without which it would not be such an achievement. It was a pleasure to work with him during all these years. I am grateful for the orientation.

My gratitude to co-advisor professor Rigoberto E. M. Morales from UTFPR, and my advisor at Colorado School of Mines, professor Amadeu K. Sum for all support during all the work and especially during my exchange period.

I am extremely grateful to my family for all the support and encouragement, especially my parents Julia and Paulo, and my sister Yuri.

To all especial people in my life, specially Livia Okumoto.

To all professors involved in my training and those involved in the project in some way.

To all my friends and laboratories involved, especially at NUEM.

To people closest to me, which one way or another pushed me and walked with me these last times, my deepest gratitude to Aluísio Wrasse, Eduardo Nunes, Guilherme Weber, José Galvão and Tiago Vendruscolo for all the help, friendship and advises.

To those who contributed to the completion of such work.

Financial support of Coordenação de Aperfeiçoamento de Pessoal de Nível Superior – Brasil (CAPES).

This doctoral thesis is dedicated especially to my beloved parents who always encouraged me, believed in me and gave me all the support needed to reach this goal.

Resumo

LONGO, Jean P. N., **Sensores para detecção de hidratos por espectroscopia de impedância elétrica**. 110 p. Tese de doutorado – Pós-Graduação em Engenharia Elétrica e Informática Industrial (CPGEI), Universidade Tecnológica Federal do Paraná (UTFPR). Curitiba, 2020.

Sensores de impedância, nos quais a substância em análise causa uma variação em uma propriedade elétrica do sensor como resistência ou capacitância, são aplicados nesse trabalho para monitorar fluidos em processos industriais. No campo de produção de petróleo e gás, uma necessidade atual é a monitoração da formação e crescimento de hidratos, que são estruturas cristalinas, as quais podem se formar nas linhas de produção em determinadas condições de pressão e temperatura. Tais substâncias podem interromper a produção causando riscos e/ou aumentando os custos. No cenário atual de instrumentação industrial, não existe uma técnica de detecção estabelecida para a monitoração da formação de hidratos em oleodutos, sendo assim, neste trabalho a espectroscopia de impedância elétrica é aplicada para esse propósito, uma vez que é uma técnica robusta, simples e de baixo custo, na qual a assinatura elétrica de cada substância em análise é avaliada. Além do uso de uma célula sensora comercial, um sensor dedicado foi projetado e construído baseado na geometria de placas côncavas com o objetivo de ser aplicado em oleodutos. Aliada a medições de impedância de 40 Hz a 5 MHz, a formação e crescimento de sólidos foi monitorada. Inicialmente experimentos estáticos foram conduzidos com substâncias conhecidas para a calibração do sensor, depois experimentos com água congelando foram realizados, uma vez que o gelo tem muitas similaridades com hidratos. Finalmente, um experimento preliminar usando uma substância modelo (tetrahidrofurano) foi conduzido para a formação de hidratos. Assim, a espectroscopia de impedância é uma técnica promissora a ser aplicada em processos de fluxo para auxiliar no monitoramento de hidratos.

Palavras-chave: Sensor de impedância. Formação de hidratos. Garantia de escoamento.

Abstract

LONGO, Jean P. N., **Sensors for hydrates detection based on electrical impedance spectroscopy**. 110 p. Doctoral Thesis – Graduate Program in Electrical and Computer Engineering (CPGEI), Federal University of Technology – Paraná (UTFPR). Curitiba, 2020.

Impedance sensors, in which the measurand causes a variation of an electrical sensor property such as resistance or capacitance, are applied in this work to monitor fluids in industrial processes. In the field of oil and gas production, a current need is to monitor the formation and growth of hydrates. Hydrates are solid crystalline structures, which may form in the oil stream under certain pressure and temperature conditions. Such hydrates may disrupt the production causing risks and/or increasing productions costs. In the current industrial instrumentation scenario, there is no established detection technique for monitoring the formation of hydrates within the pipelines. In this work, electrical impedance spectroscopy is applied for this purpose, which is a robust, simple and low-cost technique. Hence, the electrical signature of each substance under analysis is evaluated. Besides the use of commercial sensing cell, a dedicated sensor was designed and constructed based on a concave plates geometry with the aim to be applied in pipes. Allied to impedance measurements in the range 40 Hz to 5 MHz, the formation and growth of solids was monitored. Initially static experiments were carried out with known substances for sensor calibration. Water freezing experiments were also performed, since ice has several similarities with hydrates. Finally, an experiment using a model substance (Tetrahydrofuran) was performed for hydrate formation. Thus, impedance spectroscopy is a promising technique to be applied in flow processes to help in monitoring hydrates.

Keywords: Impedance sensor. Impedance spectroscopy. Hydrates formation. Flow assurance.

List of figures

Figure 1 - Complex plane representation of impedance and admittance.	23
Figure 2 - Schematic representation of different dielectric mechanism.....	26
Figure 3 - Ice permittivity for -10.8 °C.	27
Figure 4 - (a) Debye equivalent circuit, (b) Complex plane plot and (c) Real and imaginary parts of the complex permittivity.....	28
Figure 5 - Tap and deionized water permittivity according to the Debye relaxation function. ϵ' for real and ϵ'' for imaginary parts.....	29
Figure 6 - Equivalent circuit with two layers: the first represents the electrolyte and cables and the second the electrode-electrolyte interface.....	32
Figure 7 - Needle probe schematic diagram.	34
Figure 8 - Parallel-plates sensor on the walls of a vat.....	35
Figure 9 - Configuration of ring electrodes on pipe wall.	35
Figure 10 – Planned schematic diagram of the sensor with segmented receiver.....	36
Figure 11 - Helical electrode scheme.	36
Figure 12 - Interdigital sensor.....	37
Figure 13 - Schematic of two-wire sensor.....	38
Figure 14 - Wire-mesh schematic.	38
Figure 15 - Hydrates formation in pipelines. Grey represents the fluid and white represents hydrates.....	42
Figure 16 - Most common techniques for inhibition and mitigation of hydrates.	43

Figure 17 - Phase diagram of ice.	44
Figure 18 - Process of water crystallization.	45
Figure 19 - Typical geometries of short deadlegs.	46
Figure 20 - Possible hydrate challenges in deadlegs.	47
Figure 21 - Bragg grating and incident, reflected and transmitted spectra.	48
Figure 22 - Typical FBG temperature response.	50
Figure 23 - 16452A Liquid dielectric test fixture.	52
Figure 24 - Schematic representation and cross-section of the electrodes of concave plates.	53
Figure 25 - (a) Exploded view of electrical structure of the concave plate sensor and (b) dimensions.	54
Figure 26 - Details of encapsulated FBG.	54
Figure 27 - Temperature FBG calibration.	56
Figure 28 - Complete structure of sensor.	56
Figure 29 - (a) new dimensions for the concave plate sensor (deadleg sensor) and (b) electric field behavior.	57
Figure 30 - Concave plate sensor for deadleg.	58
Figure 31 - System diagram for concave plates sensor.	59
Figure 32 - Deadleg system for hydrate studies.	61
Figure 33 - Schematic overview of CSM facilities.	62
Figure 34 - Frequency versus capacitance of THF and deionized water mixture.	65
Figure 35 - Frequency versus resistance of THF and deionized water mixture.	65

Figure 36 – Static permittivity for THF and water mixtures using commercial cell. Permittivity was evaluated at 5 MHz.	66
Figure 37 - Capacitance and resistance Bode plots for ice formation fitted with $R C + C (R + R Q)$ using the commercial sensor.	67
Figure 38 - Water impedance fitted with $R C + C (R + R Q)$ using the commercial sensor.	68
Figure 39 - Ice impedance fitted with $R C + C (R + R Q)$ using the commercial sensor.	69
Figure 40 - Temperature behavior during ice formation.	70
Figure 41 - Frequency versus capacitance and resistance spectra during ice formation experiment.....	71
Figure 42 - Capacitance spectra for ice for 100 Hz, 1 kHz, 10 kHz 100 kHz and 1 MHz compared with temperature.	72
Figure 43 - Resistance spectra for ice for 100 Hz, 1 kHz, 10 kHz, 100 kHz and 1 MHz compared with temperature.	73
Figure 44 - Capacitance and resistance Bode plots for ice formation fitted with $R C + C (R + R Q)$ using the combined sensor.	74
Figure 45 - Water and ice impedance fitted with $R C + C (R + R Q)$ using the combined sensor.	74
Figure 46 - Capacitance and resistance Bode plots for hydrates formation fitted with $R C + C (R + R Q)$ using the commercial sensor.	76
Figure 47 - THF + water and hydrates impedance fitted with $R C + C (R + R Q)$ using the commercial sensor.	77
Figure 48 - Temperature behavior during hydrate formation. Chiller set point was -5 °C.	79

Figure 49 - Frequency versus capacitance and resistance spectra during hydrate formation experiment.....	79
Figure 50 - Capacitance spectra of hydrate for 100 Hz and 1 kHz compared with temperature.	80
Figure 51 - Capacitance spectra of hydrate for 10 kHz, 100 kHz and 1 MHz compared with temperature.	81
Figure 52 - Resistance spectra for ice for 100 Hz, 1 kHz, 10 kHz, 100 kHz and 1 MHz compared with temperature.	81
Figure 53 - Capacitance and resistance bode plots for hydrates formation fitted with $R C+C (R+R Q)$	82
Figure 54 - THF + water mixture and hydrates impedance fitted with $R C + C (R + R Q)$ using the combined sensor.	83
Figure 55 - Impedance plots for water, ice, THF + water mixture, hydrates and the fits plotted together.	84
Figure 56 - Glass jacketed beaker.	86
Figure 57 - Impedance spectra for standard substances using the AD5933 and deadleg sensor.	87
Figure 58 – Linear behavior of the electronics regarding the measured capacitance and the permittivity values from literature for air, oil, alcohol and water.....	87
Figure 59 - Impedance spectra for ice formation using AD5933 and deadleg sensor..	88
Figure 60 - Capacitance values for ice formation using FDC2214 and deadleg sensor.	89

List of tables

Table 1 - Relative permittivity for selected substances for 25 °C.....	25
Table 2 - Comparison between some different measurements techniques.....	39
Table 3 - Simulates and measured values of capacitance for concave plate sensor.....	55
Table 4 - Parameters obtained from fitting impedance data for water and ice for the commercial sensor.....	69
Table 5 - Parameters obtained from fitting impedance data for water and ice for the combined sensor.	75
Table 6 - Parameters obtained from fitting impedance data for THF + water mixture and hydrates for the commercial sensor.	78
Table 7 - Parameters obtained from fitting impedance data for THF + water mixture and hydrates for the combined sensor.	83
Table 8 - Calculated relative mean absolute error between data and fits	85

Nomenclature

Roman symbols*

B	Susceptance	S
C	Capacitance	F
E	Electrical field	V/m
f	Frequency	Hz
G	Conductance	S
I, i	Electrical current	A
j	Imaginary unit	-
k	Constant	-
l	Length	m
R	Resistance	Ω
T	Temperature	° Celsius
V	Voltage	V
v	Voltage	V
X	Reactance	Ω
Y	Admittance	S
Z	Impedance	Ω

Greek symbols

Γ	Boundary	-
ϵ	Electric permittivity	-

* Note that in this thesis the bold-faced variables such \mathbf{Z} or $\boldsymbol{\epsilon}$ represent complex quantity or a vector.

γ	Strain	m
σ	Conductivity	S/m
θ	Angle	rad, °
ρ	Electric charge density	C/m ³
ω	Angular frequency	rad/s
λ	Bragg wavelength	m
Λ	Period of the grating	-
n	Refractive index	-

Subscripts

0	Vacuum
A	Air
a	Absolute
FBG	Fiber Bragg grating
eff	effective
f	Final, Freezing point
g	Gas
O, o	Oil
o	Output
r	Relative
sim	Simulated
T	Total
W, w	Water
x	Unknown

Abbreviations

AC	Alternating current
CT	Computer tomography
C _p	Capacitance (F)
CSM	Colorado School of Mines
DAQ	Data acquisition
DC	Direct current
EIS	Electrical impedance spectroscopy
EIT	Electrical impedance tomography
FBG	Fiber Bragg Grating
FEM	Finite element method
fps	Frames per second
I	Ice
I _c	Cubic ice
I _h	Hexagonal ice
MEG	Monoethylene glycol
NUEM	Multiphase Flow Research Center
ppm	Parts per million
R _p	Resistance (Ω)
sI	Hydrate structure I
sII	Hydrate structure II
THF	Tetrahydrofuran
UTFPR	Universidade Tecnológica Federal do Paraná
VBA	Visual Basic for Application

Contents

1.	Introduction	19
1.1	Motivation.....	19
1.2	Objectives.....	20
2.	Theoretical background	22
2.1	Electrical impedance spectroscopy	22
2.1.1	Definitions	23
2.1.2	Dielectric relaxation.....	25
2.1.3	Double layer capacitance	30
2.1.4	Nonlinear least squares fitting	30
2.1.5	Equivalent electrical circuit model.....	31
2.1.6	Mean absolute error (MAE)	33
2.1.7	Types of sensors.....	33
2.2	Clathrate hydrates	39
2.2.1	Structure and types of hydrates.....	40
2.2.2	Similarities to ice	43
2.2.3	Deadlegs	46
2.3	Temperature measurement by FBG.....	48
3.	Sensor design, measuring systems and facilities	51
3.1	Overview	51
3.2	Impedance sensors design and construction.....	52
3.2.1	Combined sensor	52
3.2.2	Deadleg sensor	57
3.3	Acquisition systems and facilities.....	58
3.3.1	Multiphase Flow Research Center (NUEM) facility	58
3.3.2	Deadleg facility at Colorado School of Mines (CSM).....	60
3.4	Matlab algorithm	62
4.	Tests and results	64

4.1	Verification experiments	64
4.2	Ice formation monitoring using the commercial sensor	67
4.3	Ice formation monitoring using the combined sensor	70
4.3.1	Temperature.....	70
4.3.2	Electrical impedance	71
4.4	Hydrates formation using the commercial sensor.....	75
4.5	Hydrates formation using the combined sensor.....	78
4.5.1	Temperature.....	78
4.5.2	Electrical impedance	79
4.6	Applying the Relative Mean Absolute Error	85
4.7	Deadleg sensor experiments	86
4.7.1	Verification experiments.....	86
4.7.2	Ice formation monitoring.....	88
5.	Conclusion.....	90
5.1	Conclusions.....	90
5.2	Future development.....	91
	References	92
	Appendix A Experimental methodology manual.....	105

1. Introduction

This opening chapter presents the motivation and objectives of the doctoral thesis.

1.1 Motivation

Sensors based on the variation of the electric impedance of a device (resistance, capacitance or both) are widely applied to monitor plant or process parameters in industry. There are many physical and/or chemical principles which affect the electric impedance of a material in between the electrodes forming a sensing element. Industrial processes involving fluids are extreme common in many branches (such as chemical and manufacturing industry) and the need for monitoring and control such processes is steadily increasing due to the always stricter requirements on safety and efficiency.

Industrial processes have become more complex and require more and more in-depth studies to ensure continuous process improvement which in turn allows to lower production costs and to maintain plant and equipment safety. In this scenario, fluid analysis is of great importance to industry in general, since in many processes there are numerous types of fluids involved. More specifically in petroleum industry, an aspect widely discussed and studied, the flow assurance is highlighted in this scenario. Flow assurance means the field within petroleum engineering which aims at sustaining the flow of produced fluids in pipelines and is one of the major technical problems in offshore production (MACKINTOSH and ATAKAN, 2000). Many problems can occur in the flowlines with the fluid that are present there, forming plugs and disrupting the flow, for instance wax, asphaltenes and hydrates. This work will focus on the study of fluids that can harm the cited process, once any accumulation inside pipelines can result in unscheduled stoppages in production (consequently causing losses) and also can risk operating conditions, which could require extensive work to fix the issues. According to Sloan (2003), the most urgent consideration to oil and gas pipelines is the flow assurance and when hydrates form it can disrupt the flow. The development of this substance and its agglomeration are one of the major causes of pipelines blockages

(HAMMERSCHMIDT, 1934; SLOAN and KOH, 2008), that is why is so important to keep the processes outside the hydrate formation envelope.

Besides the economic problem caused directly by the production stoppage, a secondary concern is the rapidly movement (up to 300 km/h) of the hydrates plug that can be caused by any pressure gradient across the hydrate plug, leading to (in extreme cases) loss of property and even lives (SLOAN, 2003). Additionally, according to Collett (2002), the hydrates formation during drilling will drastically change the rheological properties of the fluids, being able to lead to line blockages in some cases and in others to dissociation while drilling through hydrate-bearing and possible uncontrollable gas release.

The reliable detection of these solid deposits is important as online surveillance tool to avoid the cited problems. Currently, the used techniques for hydrates detection are reliable only for laboratory application (SUM et al. 2019) or for natural gas hydrates reservoir detection outside the flow assurance field (WEITEMEYER et al., 2006), since hydrates can be a natural resource of gas (KOH et al. 2012). Aiming at field application and on the way to validation, in this perspective, the electrical impedance sensors allied to spectroscopic measurements seems to be a good candidate technique to fluid monitoring and to predict such formations, enabling a better understanding of the physical-chemical process of formation so that is possible to develop in the future more improved remediation techniques for the formation of such substances.

1.2 Objectives

In this work, the main goal is to develop a sensor capable of measuring hydrates presence in pipes without interrupting the flow. For that, impedance spectroscopy is the chosen technique and THF (tetrahydrofuran – C_4H_8O) is selected to be the guest molecule for hydrates as model fluid when working at atmospheric pressure. As hydrates are very similar to ice, therefore, firstly ice-forming experiments will be conducted. To achieve those objectives, this work is divided in two main lines.

(i) The application of impedance technique for data acquisition:

- Validation experiments;
- Ice formation monitoring;
- Hydrates formation monitoring;

(ii) The sensors design:

- Simulation;
- Construction.

As a result, with the development of these sensors, it is intended to contribute to the development of online monitoring tool for hydrates detection.

2. Theoretical background

This chapter provides essential knowledge of impedance spectroscopy, hydrates and ice as its structures, types and growth process. For hydrates the chapter goes further, exploring the inhibition process and a summary about tetrahydrofuran.

2.1 Electrical impedance spectroscopy

The electrical impedance spectroscopy (EIS) aims at determining the response of a substance electrical impedance at various frequencies. The general approach of the technique is to apply an electrical stimulus (voltage or current) to the electrode and monitor the response. This technique is a common tool in analytical chemistry. EIS is widely used in several processes of monitoring and detection. From detection of microorganisms (ALOCILJA and RADKE, 2003), bacterial concentration (CADY, 1978), analysis of human body (MIALICH et al., 2014), food quality (HARKER and MAINDONALD, 1994), cow milk adulteration (DURANTE et al., 2016), to corrosion (SEKINE, 1997), loss of coating protection (ZUO et al., 2008), estimate the state of charge of batteries (RODRIGUES et al., 2000), oil concentration (GROSSI and RICCÒ, 2017) and stability of emulsions (ROLDAN-CRUZ et al., 2016).

Because EIS may be applied over a very large range of frequencies (from 10 μ Hz to 14 GHz or higher) according to Macdonald (1992) it could be simple in theory, but often complicated in practice.

Even so there are many techniques for impedance measurements depending on system complexity, measurements range, frequency range, required accuracy, each with its advantages and disadvantages for certain conditions. At lower frequencies – up to MHz – impedance is determined using lumped circuits, which are measured by current-voltage, bridge or resonant methods (KEYSIGHT, 2016b).

In process diagnostics, EIS use is not so widespread. Here rather simpler measuring techniques are applied, for instance pure conductance or capacitance

measurements. In the field of oil and gas production, this type of measurement has been used since the 1940s, mainly due to the low cost and high measurement speed (FALCONE et al., 2009).

2.1.1 Definitions

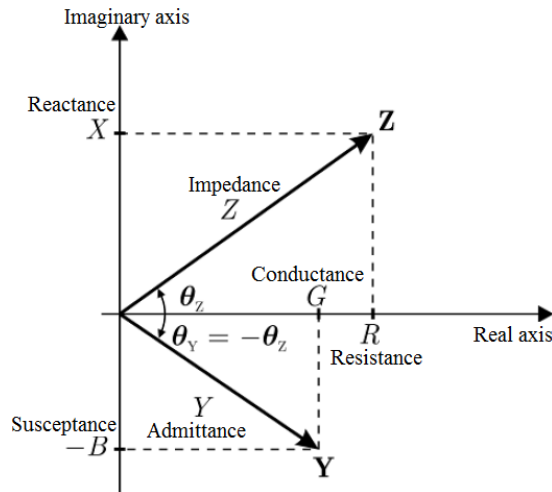
Impedance measurement is a commonly used method to characterize circuits, components, solutions and materials (WEBSTER, 1999). The Ohm's law in phasor notation give us the definition of impedance \mathbf{Z} , being ω the angular frequency

$$\mathbf{Z}(\omega) = \frac{\mathbf{V}(\omega)}{\mathbf{I}(\omega)}, \quad (2.1)$$

being \mathbf{V} the electric voltage and \mathbf{I} electric current. Inverse of impedance is known as admittance $\mathbf{Y} = \mathbf{Z}^{-1}$.

In Figure 1 it is possible to observe a representation of impedance and admittance in the complex plane.

Figure 1 - Complex plane representation of impedance and admittance.



Source: Adapted from Da Silva (2008).

Using this plane is possible to demonstrate that

$$|\mathbf{Z}| = Z = \sqrt{R^2 + X^2} \quad (2.2)$$

and

$$|\mathbf{Y}| = Y = \sqrt{G^2 + B^2}, \quad (2.3)$$

where resistance (R) and conductance (G) are the real parts, indicating the losses within the circuit and reactance (X) and susceptance (B) are the imaginary parts, measuring the reactive energy stored in the circuit on a period. In general, these quantities are frequency dependent. When the angle $\theta = 0$ the complex quantity \mathbf{Z} becomes real, once in this case $\mathbf{Z} = R$, being purely resistive.

Impedance is commonly used in electric circuits theory. However, the parameter complex permittivity is commonly used in material science, being a complex-valued parameter and denoted by ϵ .

$$\epsilon = \epsilon' - j\epsilon'' \quad (2.4)$$

In equation 2.4, there is a real part ϵ' (permittivity – sometimes referred as dielectric constant) and imaginary part ϵ'' (also known as loss factor). In a succinct manner, the real part of the complex permittivity describes the ability of a material to support an electrical field. The losses include dielectric loss due to relaxation or resonant effects in the materials as well as loss by ionic conduction.

In many cases, only the real part of eq. 2.4 is of interest and a simplest way to represent it is by the relative permittivity:

$$\epsilon_r = \frac{\epsilon}{\epsilon_0}, \quad (2.5)$$

related to the vacuum permittivity ϵ_0 (pF/m). Table 1 lists some substances and their permittivity values (for MHz range).

Table 1 - Relative permittivity for selected substances for 25 °C.

Substance	Relative permittivity (ϵ_r)
(Dry) Air	1.00
Methane	1.0008181
Ethane	1.001403
Crude oil	2.19
THF	7.52
2-propanol	20.00
Ethanol	24.00
Ethylene glycol	37.00
THF + water mixture ¹	73.10
Deionized water	78.00
Pure ice (-5 °C)	95.00

Source: Adapted from Buckley and Maryott (1958), Kopp (1962), Morris and Davidson (1970), Csikós et al. (1982), Kumbharkhane et al. (1996), Chen et al. (1997), Folgerø (1998) and Haynes (2016)

¹Water 80% and THF 20%

The more distant the relative permittivity between two substances the easier it is for the measuring equipment to distinguish the substances under analysis (e.g. air and deionized water). On the other hand, the closer the values the more difficult the distinction (e.g. methane and ethane – to be more specific, according to Haynes (2016) the methane permittivity is 1.0008181 and ethane is 1.001403). For the commercial available equipment, it is not possible to distinguish these substances.

2.1.2 Dielectric relaxation

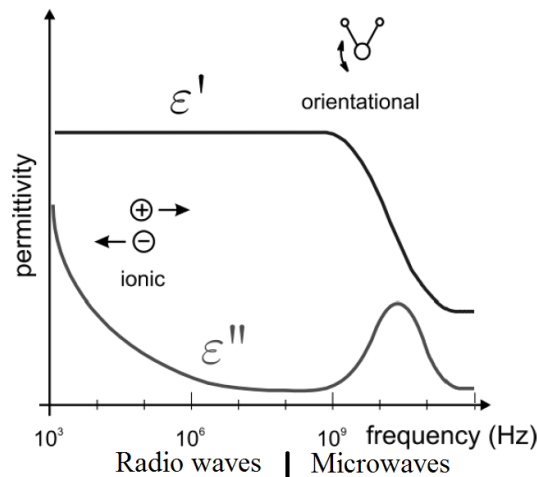
Normally is complex to determine the overall electrical behavior of substances, once a number of strongly coupled processes occurs. Impedance spectroscopy is the method of choice for characterizing this behavior (BARSOUKOV and MACDONALD, 2005). When a substance receives an electrical stimulus, many fundamental process take place on a microscopic level, leading to the overall electrical response.

Dielectric relaxation is a concept that involves these microscopic process. Usually when the frequency applied in a substance is increased, it has a dielectric relaxation, in which ϵ' decreases. Several polarization effects (the atom or molecule of

a material under external electric field forms an electric dipole) or dielectric processes can occur in a single fluid, contributing to its permittivity as a whole.

Each dielectric mechanism has a characteristic frequency of response. Over the low-frequency spectrum (kHz range) the nonrelaxation-type ionic conduction losses are readily perceptible and decreases with frequency, as can be seen in Figure 2.

Figure 2 - Schematic representation of different dielectric mechanism.

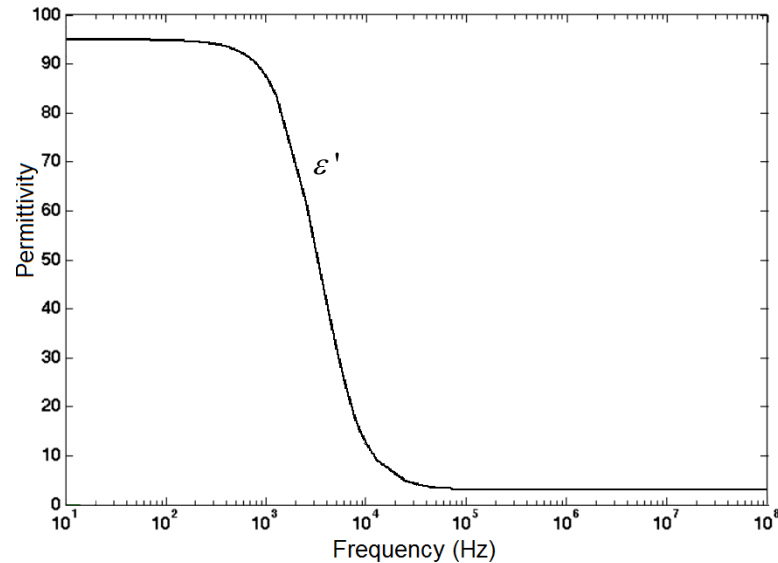


Source: Adapted from Adapted from Keysight (2019).

According to Macdonald (1987), it was verified that a single relaxation process characterizes the dielectric mechanism behavior for many liquids from low frequency up to the microwave frequency region.

Unlike the other substances that pass through the phenomenon of the relaxation only at higher frequencies (in the microwave frequency, i.e. from 200 MHz or more), for ice, this phenomenon occurs in the order of kHz, according to Figure 3.

Figure 3 - Ice permittivity for -10.8 °C.



Source: Adapted from Leitzke (2014).

Barsoukov and Macdonald (2005) also quotes that when an insulating material receives an electric field \mathbf{E} , the polarization process \mathbf{P} will occur and may be divided into two parts according to the time constant of the response. The first one is the almost instantaneous polarization, which occurs due to the displacement of the electrons with respect to the nuclei. This defines the high-frequency dielectric constant ϵ_{∞} :

$$\epsilon_{\infty} - 1 = \frac{\mathbf{P}_{\infty}}{\mathbf{E}\epsilon_0} . \quad (2.6)$$

The time constant of this process is about 10^{-16} s.

The second one is a time-dependent polarization $\mathbf{P}'(t)$ due to the orientation of dipoles in the electric field. The resulting total polarization \mathbf{P}_s occurs if the field remains in place for an infinitely long time and it defines the static dielectric constant ϵ_s :

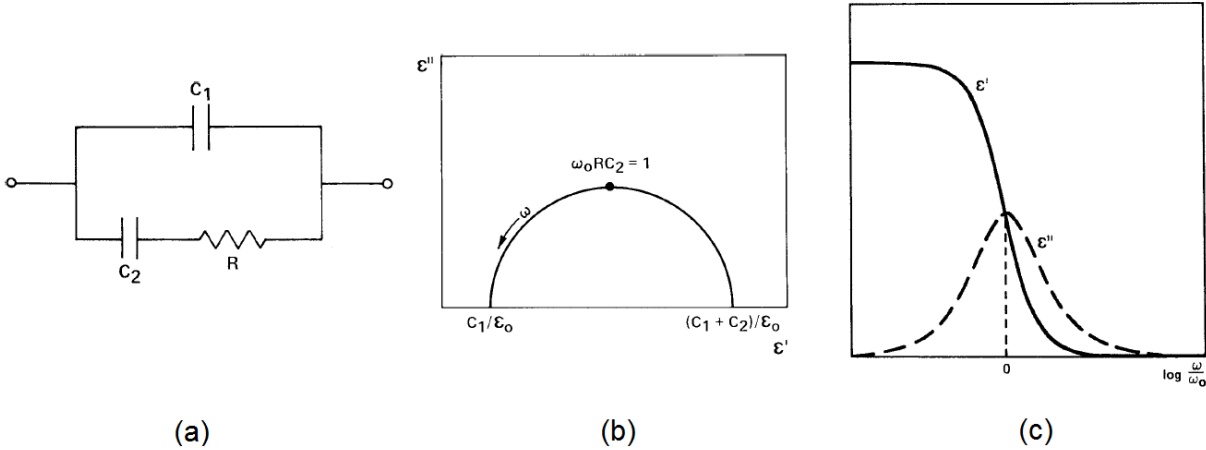
$$\epsilon_s - 1 = \frac{\mathbf{P}_0}{\mathbf{E}\epsilon_0} . \quad (2.7)$$

According to the mathematics exemplified by Macdonald (1987), the expressions may be rewritten in terms of the complex dielectric constant $\epsilon = \frac{Y}{j\omega\epsilon_0}$:

$$\epsilon - \epsilon_\infty = \frac{\epsilon_s - \epsilon_\infty}{1 + \omega^2\tau^2} - j \frac{\omega\tau(\epsilon_s - \epsilon_\infty)}{1 + \omega^2\tau^2} . \quad (2.8)$$

The real and imaginary parts of this expression are the Debye relaxation relations (MACDONALD, 1987). This model is frequently used to explain the dielectric behavior of materials. For the interpretation of the physical phenomena describing the relaxation process, the equivalent circuit is also used. In Figure 4 (a) it is possible to observe the Debye equivalent circuit, (b) complex plane plot of the frequency dependence of the complex permittivity modeled by the circuit (a), and (c) is the real and imaginary parts of the complex permittivity as a function of normalized radial frequency.

Figure 4 - (a) Debye equivalent circuit, (b) Complex plane plot and (c) Real and imaginary parts of the complex permittivity.



Source: Macdonald (1987).

To correctly separate the real and imaginary parts, it is necessary to add the conductivity term, once many liquids contain a conduction effect, which may even be the result of impurities. Thus, the model can be written as

$$\epsilon = \epsilon_\infty + \frac{\epsilon_s - \epsilon_\infty}{1 + j\omega\tau} - j \frac{\sigma}{\omega\epsilon_0} , \quad (2.9)$$

having the real and imaginary parts separated in

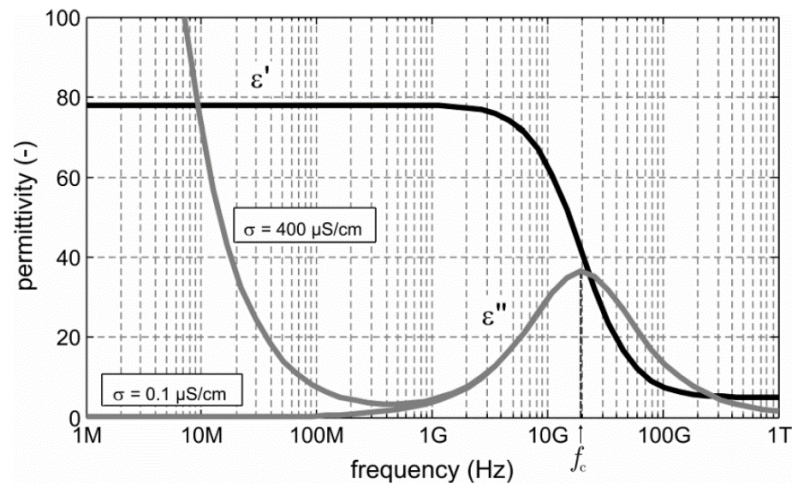
$$\epsilon' = \text{Re} \{ \epsilon \} = \epsilon_{\infty} + \frac{\epsilon_s - \epsilon_{\infty}}{1 + \omega^2 \tau^2} \quad (2.10)$$

and

$$\epsilon'' = \text{Im} \{ \epsilon \} = \frac{\sigma}{\omega \epsilon_0} + \frac{\omega \tau (\epsilon_s - \epsilon_{\infty})}{1 + \omega^2 \tau^2}. \quad (2.11)$$

For water at 25 °C, the real and imaginary parts of equation can be plotted as in Figure 5, according to Debye relaxation function (2.9 and 2.10), for two arbitrary conductivity values: for tap water $\sigma = 400 \mu\text{S}/\text{cm}$ and for deionized water $\sigma = 0.1 \mu\text{S}/\text{cm}$.

Figure 5 - Tap and deionized water permittivity according to the Debye relaxation function. ϵ' for real and ϵ'' for imaginary parts.



Source: Da Silva (2008).

However, in nature not all fluids obey the Debye equation and can have more than one relaxation time. Thus, a widely used function is the Cole-Cole equation

$$\epsilon = \epsilon_{\infty} + \frac{\epsilon_s - \epsilon_{\infty}}{1 + (j\omega\tau)^{1-\beta}}, \quad (2.12)$$

where, according to Macdonald (1987), β is a parameter which gives a measure of the broadening in the peak of ϵ'' , indicating a distribution of relaxation times. Therefore if $\beta=0$ we get back to Debye equation (2.9). In this work we will see a similar behavior for some data and we can fit it using these equations.

2.1.3 Double layer capacitance

The double layer capacitance has been studied due to its importance within a wide number of areas, e.g. geophysics, colloid science and electrochemistry, which is in our interest. Besides, it can possibly be applied for energy storage and power devices in future as super capacitors (VANGARI, et al., 2013 and CHEN, et al., 2014).

According to Stojek (2010), at any electrode immersed in an electrolyte solution, a specific interfacial region is formed and the electrical properties of such a layer is important, since they significantly affect the electrochemical measurements. This phenomenon can be viewed as a capacitor, and the so-called double layer capacitance normally occurs on the surface of an object exposed to a fluid, and in our case, under an electric field. Due to the electrical charge, two layers can be observed: the first one consists of ions adsorbed onto the object due to electrical field and the second one due to attracted ions to the surface charge via the Coulomb force. The first observation of this phenomenon was made by Helmholtz (1853) and he described the first model for this subject. A more recent work from Aoki (2016) shows the frequency-dependence of electric double layer capacitance and describes why for low frequencies this effect is stronger and can disturb our measurement. For the variables that can affect the double layer capacitance, we can mention the conductivity (MORITA et al., 1992), the type and size of solvent molecules (ARULEPP et al., 2004), the size of the cations (DAMASKIN, et al., 2011) and anions (KURIG et al., 2011). If non-ionic substances are adsorbed on carbon electrodes, the capacitance can vary with the dc-potential (KIM et al., 2003) and according to Hou (2014), the double layer capacitance decreases generally with an increase in frequency and the biggest variations are often found at ac-frequency, also called the frequency dependence of capacitance or frequency dispersion.

2.1.4 Nonlinear least squares fitting

This form of least squares analysis can be used to fit a set of m observations with a model that is non-linear in n unknown parameters. Also known as nonlinear regression

analysis, it refers to equations that are nonlinear in their parameters and has to rely on iterative procedures to find the best fit, in other words, according to Johnson and Frasier (1985) it is a numerical method for choosing an optimal set of parameters of an equation which describes a set of data points.

In order to fit the equations, which can also be with complex numbers, first is necessary to give a guess (starting or initial values) for the parameters. The number of parameters depends on each case and these will be changed during every step of the regression process and the algorithm will stop when it considers the measured and calculated values good enough according to the model and other predefined settings, depending on each application.

For a review of different methods for nonlinear fitting problems check Bevington and Robinson (2003), for the commonly used numerical procedures find out Johnson and Frasier (1985) and for a step by step about how to perform fitting data with nonlinear regression check Motulsky and Christopoulos (2003).

In this work, the permittivity values that we use are complex and the model is the one that follows in the next section (2.1.5). Furthermore, more practical explanations about the application of this method in this work can be found in section 3.4.

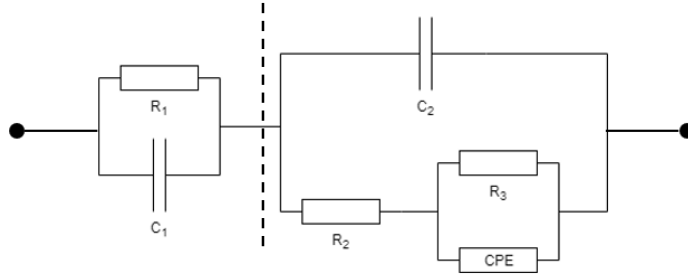
2.1.5 Equivalent electrical circuit model

A very common approach to analyze a phenomenon in electrical engineering is the use of an equivalent electrical circuit. Normally the circuit can simplify the calculations and help to understand the behavior of many events. In the most cases, the use of common elements (resistors, capacitors and inductors) is enough to analyze several phenomena, however more complex equivalent circuits should be used to describe more complex occurrences.

The Randles circuit (RANDLES, 1947) consists in a parallel resistor and capacitor in series with another resistor and this model can be adapted and have widely been applied in several fields as in electrochemical systems such as batteries, fuel cells and super capacitors (RAHN, et al., 2013 and ALAVI, et al., 2015), biomedical engineering (MIHAJLOVIĆ, 2015), corrosion monitoring (RIBEIRO, 2016), polymer degradation (FERNÁNDEZ-SÁNCHEZ, 2005) and others.

For our specifically data, the adapted Randles circuit came from Bannwart *et al.* (2006) who used the model to characterize fiber membranes. In our case, the membrane was removed from the circuit and the equivalent circuit model is showed in Figure 6.

Figure 6 - Equivalent circuit with two layers: the first represents the electrolyte and cables and the second the electrode-electrolyte interface.



Source: Personal collection.

The circuit shows a typical circuit for lossy dielectric liquids (R_1 , C_1) as well as an electrode-electrolyte interface, consisting of the double layer capacitance (C_2) in parallel with the leak of charges through the double layer due to electrochemical reactions taking place at the electrode interface. The parallel path is known as the “charge transfer” resistance (R_2). In series with that, an additional resistance due to diffusion is present (R_3). Once we have a non-ideal diffusive behavior, it is possible to use a constant phase element (CPE or Q). The constant phase element behavior is basically an imperfect capacitor and is normally used as an equivalent electrical component that models the double layer capacitance. To a better understanding of the general impedance of the proposed equivalent circuit, if we can calculate the impedance of a capacitor by $Z_C = \frac{1}{j\omega C}$ then we can calculate it for the CPE using $Z_{CPE} = \frac{1}{(j\omega C)^n}$ being $0 < n < 1$. Then, from the equivalent circuit we can get to the impedance equation

$$Z = \frac{R_1}{1 + j\omega\tau_1} + \frac{R_2 + \frac{R_3}{1 + (j\omega\tau_3)^n}}{1 + j\omega\tau_2 + \frac{j\omega\tau_4}{1 + (j\omega\tau_3)^n}}, \quad (2.13)$$

being $\tau_1 = R_1 C_1$, $\tau_2 = R_2 C_2$, $\tau_3 = R_3 Q_3^n$ and $\tau_4 = R_3 C_2$.

2.1.6 Mean absolute error (MAE)

In order to measure how good the fits are, we can calculate the mean absolute error (MAE), which measures the average magnitude of the errors in a set of forecasts (our fits in this case), without considering their direction. Basically, it measures the error between the measured data and a given fit. Using the MAE we obtain a score which means that all individual differences are equally weighted in the average. The equation applied in this work is an adaption for a relative value, i.e. MAE%:

$$\text{MAE}\% = \frac{1}{N} \sum_{j=1}^N \left| \frac{y_j - \hat{y}_j}{y_j} \right| \cdot 100\% , \quad (2.14)$$

where y is the measured data, \hat{y} is the fitted value and N the number of data points. As we are not concerned with the outliers for our measurements, the method can be a good choice, since it is not sensitive towards outliers. While the method has their limitations, it is a simple tool for evaluate a fit accuracy and can be used without knowing anything about the fit.

Normally the smaller the better, however a relatively high value for the MAE (as will be seen in some of our results, for instance) is not necessarily bad. The most important is to be able to draw consistent conclusions from the value which can be compared with other fits.

2.1.7 Types of sensors

Since the impedance is a complex quantity, two parameters need to be determined, the magnitude and phase or the real part and imaginary part of measured voltages or currents. Basically the simplest principle for understanding the technique is to apply electric stimulus on an electrode and observe the response on the other electrode, as already mentioned.

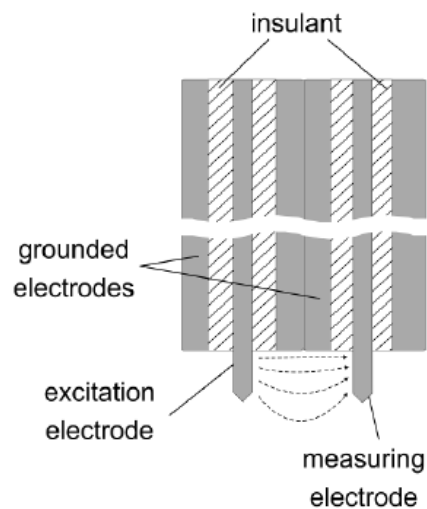
There are three basic types of electrical stimuli that can be used in impedance measurements: the most common is to measure the impedance by applying a pure sine wave and measuring the phase shift and amplitude - or real and imaginary parts of the current resulting. The second approach is to apply a transient voltage (a pulse or a step function) and the last stimulus that can be used is a voltage signal composed of random (white) noise and measure the resulting current.

The last two approaches are considered more complicated because they are classified as broadband measurements. Therefore, they require complex generation and processing of signals, making it difficult to measure at high speed. Thus, the first approach is the most appropriate for our applications.

Used for measurement and imaging of two-phase flows, the impedance techniques have specific applications for detection of each phenomenon that one wants to capture. The following will briefly describe some of probes used in these techniques.

A used probe to measure the phase present at a certain point in the cross-section of the pipes are the needle probes (CHANSON, 2002). They explore the difference of some physical property between phases, such as electrical permittivity or conductivity. By moving them in space it is also possible to determine the average void fraction of an area or volume. As disadvantages we can mention the fact that they are intrusive and have point measure. Figure 7 shows a schematic of a needle probe.

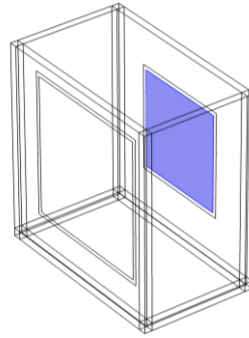
Figure 7 - Needle probe schematic diagram.



Source: Da Silva (2008).

There are also non-intrusive probes such as those of parallel-plates (Figure 8), one of the simplest geometries in which the plates can be rectangular or other geometric shape, such as circular as in the case of the commercial sensor from Keysight (illustrated in section 3) or those described by Ceccio and George (1996) in their review analysis on impedance techniques.

Figure 8 - Parallel-plates sensor on the walls of a vat.

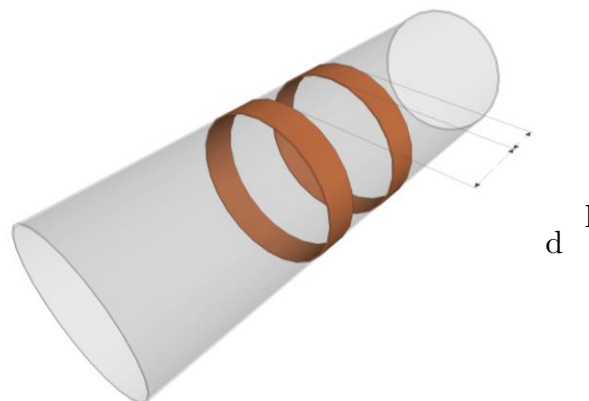


Source: Personal collection.

So-called capacitive probes (based on the difference in electrical permittivity of the substances or phases) are, in short, suitable for measuring non-conductive phases, whereas conductivity probes (based on the difference in electrical conductivity) are more appropriate for conductive substances or phases. These probes, besides being cheap, achieve a high acquisition rate, but the capacitive one takes advantage of not having to be in direct contact with the sample. For such probes there are several possible arrangements, as the ring electrodes (Figure 9).

In such a configuration, according to Ismail and Ahmed (2008), the lower the distance d between the rings, the greater the sensitivity, allowing a greater spatial resolution (when compared to the electrode of concave plates, which will be described more appropriately in section 3.2).

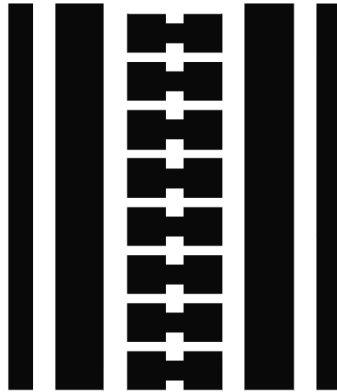
Figure 9 - Configuration of ring electrodes on pipe wall.



Source: Personal collection.

A variation of this geometry used for direct flow imaging was used by Wrasse (2015) and has two transmitter rings, but the receiver is segmented all surrounded by guard electrodes (Figure 10), and each segment is interrogated by a fast and multiplexed electronics, eliminating the need for images reconstruction.

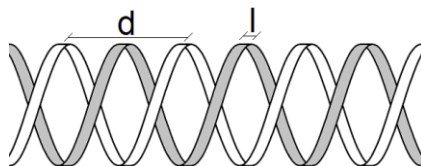
Figure 10 – Planned schematic diagram of the sensor with segmented receiver.



Source: Adapted from Wrasse (2015).

Another possible arrangement option is the helical (Figure 11). As the name already suggests, the two electrodes are arranged in a helicoid shape, arranged so that in the cross section of the tube one faces the other. In this case, the distance d represents the pitch of the spiral. Through simulations, Ye et al. (2011) shows that the spatial sensitivity can be improved by using guard electrodes between emitter and receiver. However, the length of the conductors should be about five times higher than that of other arrangements, so that the sensitivity is comparable to the others (GREGORY and MATTAR, 1973).

Figure 11 - Helical electrode scheme.

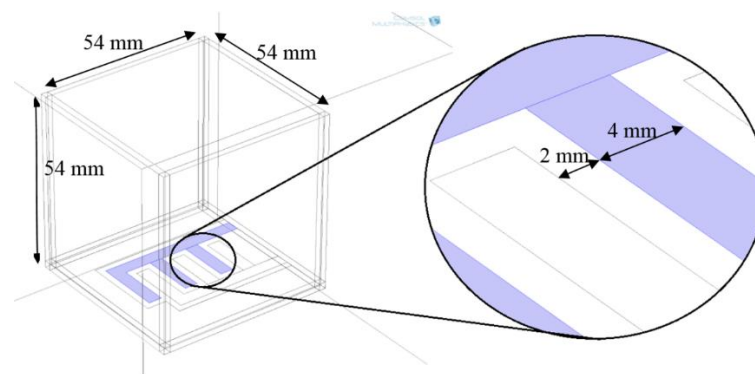


Source: Personal collection.

However, it is worth noting that, regardless of the chosen arrangement, the electrodes must be wrapped by a shielding conductor, to avoid that the measurement is interfered by external phenomena. In order for the capacitance changes to be minimal, such conductor must be grounded and disposed at a minimum distance from the measuring electrodes (ELKOW and REZKALLAH, 1996).

In addition to the aforementioned geometries, there are also interdigital sensors, used to measure the deposition of solids (wax, for example), especially in walls (LONGO et al., 2014), whose geometry was deeply simulated and later optimized by Longo (2015) which can be seen in Figure 12, and subsequently was used for the detection of ice formation (LONGO et al., 2016).

Figure 12 - Interdigital sensor.

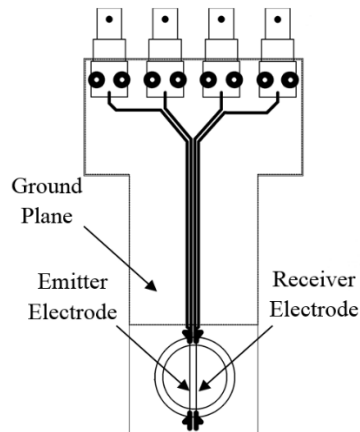


Source: Longo (2015).

The same author proposes a sensor of two wires for measurements in the cross-section of pipes, according to the schematic showed in

Figure 13. Waltrich et al. (2013) applied this type of arrangement to measure biphasic flow and Longo (2015) applied in the detection of hydrate formation in pipelines.

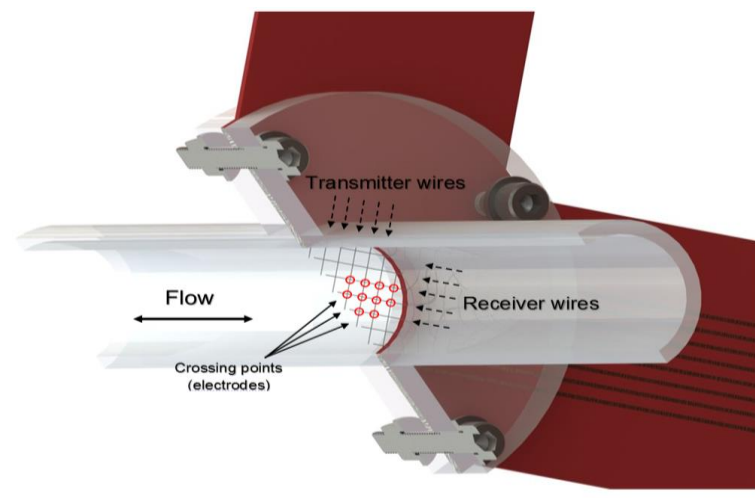
Figure 13 - Schematic of two-wire sensor.



Source: Adapted from Longo (2015).

However, for a better measurement, especially of multiphase flows (fluid flow consisting of more than one phase or component), combining the possibility of imaging, a widely used intrusive sensor is the resistive wire-mesh first proposed by Prasser et al. (1998) based on conductance measurements and later by Da Silva et al. (2007) proposed the capacitive one, which has high temporal and spatial resolution. This configuration has 2 layers of wires stretched over a pipe cross section, forming a mesh. The first layer is of emitters wires and the second of receivers and the layers are separated from each other by a small axial distance. Figure 14 illustrate the principle of work of this sensor.

Figure 14 - Wire-mesh schematic.



Source: Adapted from Dos Santos (2015).

There are other techniques to measure the permittivity like the transmission line, the free space and the resonant cavity technique and the Table 2 will bring to us the main advantages and disadvantages of each technique.

Table 2 - Comparison between some different measurements techniques.

Technique	Pros	Cons
Transmission line	<ul style="list-style-type: none"> -Can measure solids and liquids -High frequency -Anisotropic material (material that has different physical properties in different directions, e.g. wood) 	<ul style="list-style-type: none"> -Sample preparation is difficult -Cannot be used for few GHz, due to practical sample length limitation
Free space	<ul style="list-style-type: none"> -Wide frequency range -Non-contacting -Easy sample preparation -Useful for high temperature 	<ul style="list-style-type: none"> -Diffraction problem (from material edges) -Low and limited by practical sample size
Resonant cavity	<ul style="list-style-type: none"> -Can measure solids and liquids -Most accurate method -Non repetitive calibration procedure -High temperature capability 	<ul style="list-style-type: none"> -Measurements at only single or at resonant frequency -Suitable for small samples

Source: Adapted from Gregory et al. (2006), Jha et al. (2011), Keysight (2019), Venkatesh and Raghavan (2005) and Wee et al. (2009).

2.2 Clathrate hydrates

In nature, hydrates are composed by the most part of water (at least 82%) and another component, like a gas such as methane which is enclosed in a cage-like fashion. Hydrates are crystalline solids and the guest molecules are trapped in cavities of water composed by hydrogen-bonded water molecules. These crystalline hydrates were discovered by Faraday (1823) and only more than 100 years later Stackelberg and Müller (1951b) and Pauling and Marsh (1952) could determine this structure.

In the 1950s, von Stackelberg and co-workers summarized many experimental data about x-ray diffraction and the interpretation of this early experiments - von

Stackelberg (1949, 1954, 1956), von Stackelberg and Müller (1951a,b), Claussen (1951a,b), and Pauling and Marsh (1952) - leading to the determination of two structures of hydrate crystal: sI and sII. Whereas these cubic structures consist of two types of cavities, small and large cages (SLOAN, 1998). Later, a number of crystallographic studies were performed in those structures (MCMULLAN and JEFFREY, 1965 and MAK and MCMULLAN, 1965). According to these studies, hydrates are members of the class of compounds labelled “clathrates” (POWELL, 1948), that means “to engage”, and according to Sloan and Koh (2008), the clathrate hydrates are ice-like inclusion compounds that are formed when small guests are enveloped by hydrogen-bonded water cages in a crystal lattice.

2.2.1 Structure and types of hydrates

If the water is cooled down, the molecules reorganize and in a certain point of pressure and temperature, the ice is formed. There is a lot of ice structures (section 2.2.2), which depends of some factors to be formed and the most common is the hexagonal ice (I_h). However, under suitable conditions – generally low temperature and high pressure – if there is a guest molecule in the mixture, other structures can be formed. This is called hydrates cages, and these cavities are not found in liquid water, only in hydrates. As well as ice, hydrates can form several types of structures and the most commons are structure I (sI), formed by methane, ethane and cyclopropane and structure II (sII), formed by hydrogen, nitrogen, oxygen, propane, isobutene, cyclopentane and tetrahydrofuran.

Hammerschmidt (1934) carried the first work focused on an industrial application of the hydrates. The paper presented a study on gas pipes clogs during winter months, demonstrating that this problem was caused by the hydrate formation, and not by ice formation, as previously thought.

More significant studies are useful in describe details of hydrates, such as its structure, cage occupancies, formation/dissociation mechanisms, composition and molecular dynamics, as can be seen in Sum et al. (1997), Seo et al. (2002) and Sloan (2004).

The hydrate nucleation is an associated phenomenon with hydrates formation, which is a microscopic process, involving tens of thousands of molecules (MULLIN, 1993). When small clusters of water and gas grow to reach the critical size triggering

continuous growth, this phenomenon occurs. Good reviews on the nucleation process are found in Kashchiev and Firoozabadi (2002a,b).

Another observed process is the called memory effect. Hydrates store a memory of their structures when melted at moderate temperatures. Thus, the secondary formations (when the mixture reaches the proper temperature and pressure) are facilitated and occur quicker than when the phenomenon first occurred. This effect has significant implications industry wide, as once formed, if the removal of water is not complete, the hydrate will have a fast reconstruction (SLOAN and KOH, 2008).

a) Growth process and plugs of hydrates

Basically, when the conditions are conducive to hydrates formation, there are a few steps until a plug formation:

- a) Growth of first crystal;
- b) Growth of a hydrate film on the water – hydrocarbon interface;
- c) Growth of multiple crystals in an agitated system and;
- d) Growth of metastable phases.

A representation on how hydrates plugs are formed is shown in Figure 15 for condensate gas flow in pipelines. What happens in each of the five steps is detailed as follows:

I- Hydrates start nucleation at inner surface of the pipelines and starts deposition. It normally happens when water concentration is high in the flow (>7 ppm), which results in a deposition scattered along the pipe;

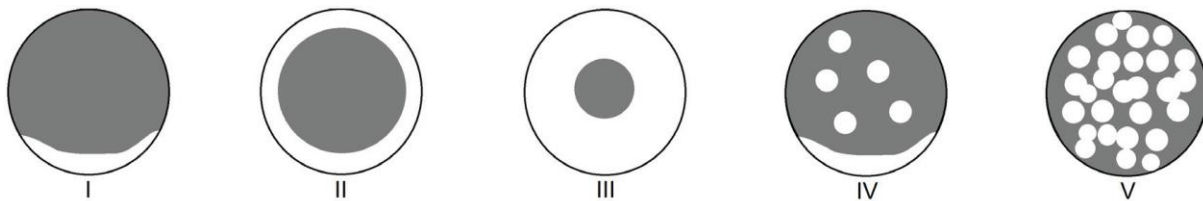
II- After nucleation in inner walls, hydrates rapidly grow and occupy the entire circumference of the pipe;

III- As the deposit grows, the useful diameter decreases;

IV- The great deposit grows until it is disturbed by some kind of phenomenon, such as harmonic resonances, density difference, slugs, among others. The deposit is not mechanically stable due to the disturbance, so it detaches from the walls and flows through the duct as hydrate particles;

V- At this point, hydrate particles end up sintering and preventing the normal flow of crude oil in pipelines.

Figure 15 - Hydrates formation in pipelines. Grey represents the fluid and white represents hydrates.



Source: Adapted from Sloan (2010).

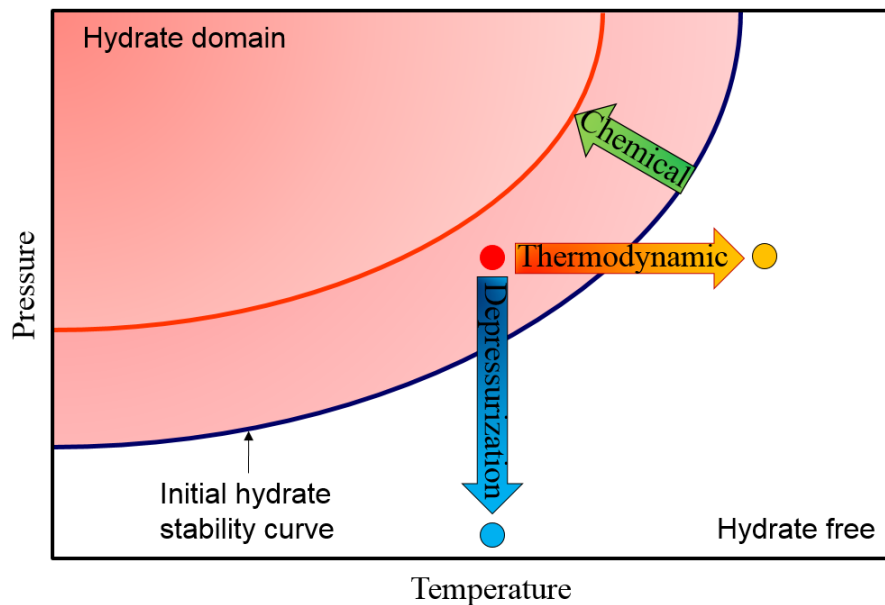
b) Inhibition and mitigation of hydrates

The perfect way to avoid hydrate formation would be to remove all the water from the systems, but in most cases this is not feasible. Thus, the alternative is the use of inhibitors. Salts and alcohols can reduce the amount of available water in the system when solubilized, hindering formation and according to KARAMODDIN and VARAMINIAN (2014), salts can be stronger inhibitors. Another way to avoid hydrates formation is the use of thermodynamic inhibitors which changes the pressure and temperature of formation, shifting out the operating condition of the stable hydrate region. Also, the MEG (Monoethylene glycol) and methanol are common thermodynamic inhibitors (SLOAN, 1998).

Once temperature is the key factor for formation, it is possible to insulate the pipelines in order to minimize thermal losses, however this is not a very effective technique in mitigating the hydrate risk (GUO et al., 2014). A better way working in temperature factor is the electric heating (LERVIK et al., 1997), but this is a very expensive method and must be used wisely.

The other key factor is the pressure, thus the depressurization of the pipeline to melt the hydrate plug is another technique, yet this potentially produces a high differential pressure across the plug, which can reach very high velocities, resulting in fatalities, equipment damage and line ruptures (SLOAN et al., 2010). Figure 16 illustrates the most common inhibition and mitigation of hydrates techniques.

Figure 16 - Most common techniques for inhibition and mitigation of hydrates.



Source: Adapted from Longo (2015).

Without the use of any preventive or remediation technique, the system is in the red dot of the figure. By using chemical inhibitors, the hydrate stability curve is shifted, since the thermodynamic inhibitors move the operation point at a higher temperature, and the depressurising decreases the pressure of the system, causing it to be outside the hydrate domain.

2.2.2 Similarities to ice

Ice and hydrates are similar once both are formed basically by water. According to Tse et al (1983), these structures are broadly similar regarding to numerical simulations for photon densities of states, which explains the close similarity of their infrared spectra and heat capacities.

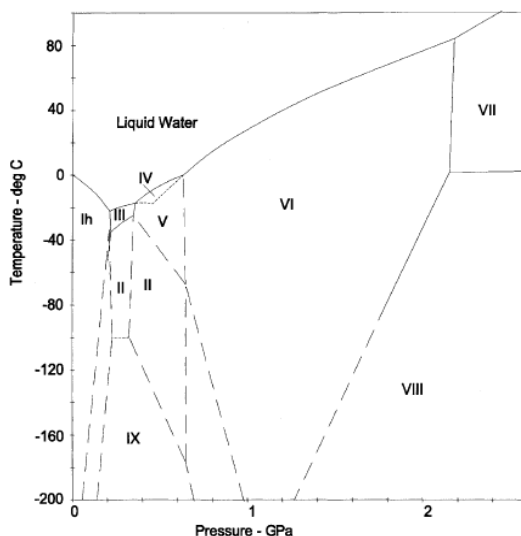
Using ultrasonic pulse transmission, Helgerud et al (2009) conclude that there are several similarities between ice and hydrates. According to the authors, wave speeds differ less than 3% between material and shear wave speed decreases with increasing axial pressure.

Ice is a crystalline structure transparent to visible light and there are many different crystal structures of ice (at least 9), the most common is the ice I, formed at ordinary (low) pressures. This structure has two variants: the hexagonal ice Ih and the cubic ice Ic. The first one has the shape of snowflakes, obtained by freezing water and

the second one is formed by depositing vapour at low temperatures ($-130\text{ }^{\circ}\text{C}$) (SCHULSON, 1999).

Figure 17 shows the phase diagram of ice. No other substance exhibits such a variety of forms to exist. However, only the hexagonal ice is found naturally.

Figure 17 - Phase diagram of ice.



Source: Adapted from Akyurt et al. (2002).

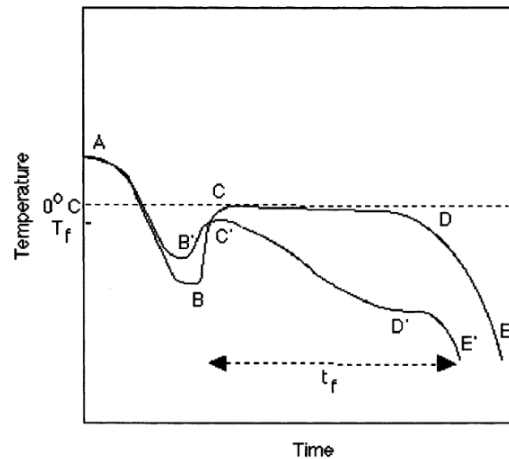
Some works can be consulted for more information on "unnatural" structures (formed or under very low temperatures or high pressures) of ice, such as Eisenberg and Kauzmann (1969), Fletcher (1970), Loban (1998) and Koza (1999). The structural versatility of the water molecule is attested by the large number of different solid phases.

Molecular forces cause water to behave different of the most substances when it is frozen into ice. Water become less dense as it is cooled below $4\text{ }^{\circ}\text{C}$ and begins to expand. The density of most liquids increases as they freeze, however, according to Ludwig (2001) water expands by about 11%, and it allows a sheet of ice to float on liquid water.

To review the freezing process, it is possible to observe Figure 18 which shows the relationship of time-temperature for freezing of pure water (ABCDE) and aqueous solution (AB'C'D'E'). Being T_f the freezing point, the first phenomena is the

supercooling, from A to B or B'. Pure water can be supercooled by several degrees before the nucleation begins.

Figure 18 - Process of water crystallization.



Source: University of Guelph (2000).

At point B or B' the system nucleates and releases its latent heat faster than the heat that is being removed from the system. The temperature increases essentially instantly to the initial freezing temperature T_f at point C or C'. In pure water, from point C to D, the crystal growth is occurring and the system will not cool until all water has crystallized into Ih ice. At point D the system already lost all latent heat and after crystallization is completed the temperature drops to E as sensible heat is released.

In these conditions, normally Ih ice is formed, and it may form as a bulk. According to Macklin and Ryan (1965) this happens because the latent heat can be dissipated more easily within the bulk of the liquid than at the surface. In addition, the behavior of rapid physical state change (liquid to solid) after supercooling (will be noted in section 4.3.1) can be attributed to the hydrogen bond angles model building, naturally present in water molecular structures. That make it easy for them to share faces and edges to form a different structure. Consequently, they are able to link up with one another more readily than others substances, on the average. Therefore, the ideal unstrained structures find it advantageous to clump together. As temperature declines, the polyhedral (a network pattern of water molecules) become more and more frequent since they incorporate stronger hydrogen bonds. As their concentration rises,

they will aggregate under the influence of the cited mean attraction to form larger and larger clumps or clusters (STILLINGER, 1980).

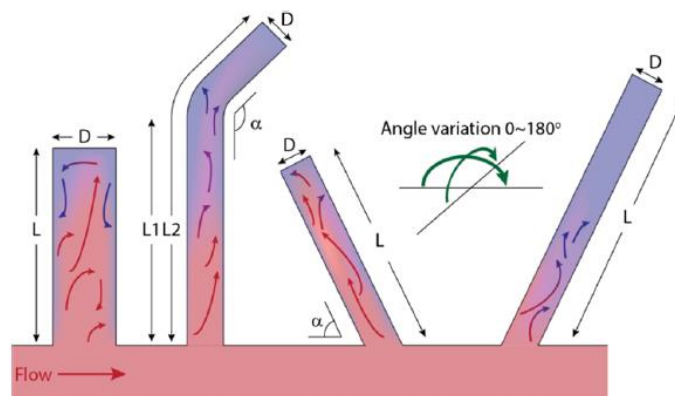
Regarding dielectric constant, according to Bernal and Fowler (1933), for sufficiently low frequencies, the permittivity of even quite cold ice can reach large values, possibly even values larger than the ordinary values for water. For sufficiently high frequencies the dielectric constant of water falls below its constant low-frequency value, but only at higher frequencies for higher temperatures.

2.2.3 Deadlegs

Deadleg is a portion of a pipe where the fluids have very low velocity or there is no flow. This inactive pipe is used to special services like fluids injection (hydrate inhibitor for instance: methanol, ethylene glycol, ...), depressurization and is normally connected to an active pipe that carries the main stream. As deadlegs are normally used for these services, hydrate blockages in them can restrict the proper management of the pipeline, which can lead to several flow assurance problems.

The diameter of the deadlegs can vary from millimetres (impulse or transmitter lines) to tens of inches (production and export lines). Knowing that, it is possible to categorize deadlegs in short (length-to-inner diameter ratio is lower than 100) and long (when this ratio is more than 100). Besides that, the angle in relation to the main flow line may vary according to each design and it is easily seen on the schematic drawn by Kinnari et al (2017) in Figure 19.

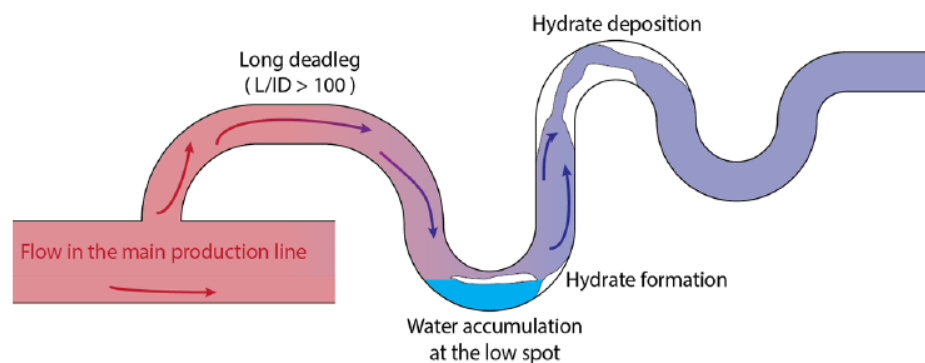
Figure 19 - Typical geometries of short deadlegs.



Source: Kinnari et al. (2017).

Long deadlegs are more vulnerable to hydrates formation once they can be colder and with more low spots (which allow water accumulation) than short deadlegs (Figure 20). In order to avoid hydrates in these long dead portions of the pipes, normally some valves are designed to isolate such deadlegs from the main system. However, due to cost issues, such valves are easily cut off. A very interesting work which studies the characteristics of flow in horizontal deadlegs can be read in Habib et al (2005b) The authors perform experiments and CFD (computational fluid dynamics) simulations to study the behavior of the flow in different sizes (length/inner diameter) of deadlegs.

Figure 20 - Possible hydrate challenges in deadlegs.



Source: Kinnari et al. (2017).

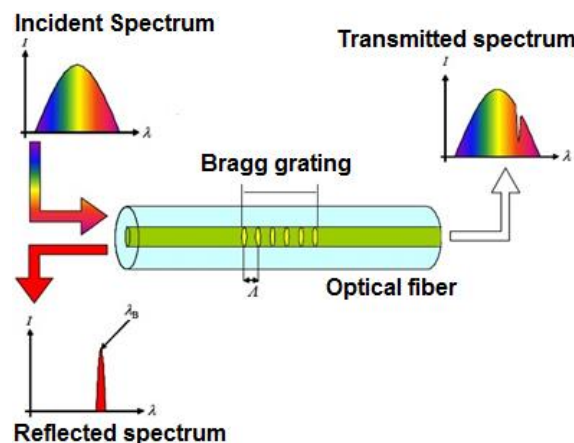
Like already said, inside this “dead” portion of the pipe, the hydrate risk is higher than in the pipe and according to Habib et al (2005a) deadlegs should be avoided whenever possible in the design of piping systems. If it is not possible, the best solution will be project the length of the inactive pipe as short as possible to avoid stagnant or low velocity fluids, even though in the oil and gas industry, deadleg corrosion presents the highest percentage of internal damage to pipelines due to flow pattern, which causes emulsified water precipitation out of the crude. Besides the ratio between length and diameter, the position and geometry of the deadleg can also influence the characteristics of the flow inside it. And, according to Craig (1996), once water begins to drop out of solution onto the metal surface, wettability (the preference of a liquid to be in contact with a solid surrounded by another fluid) would become the controlling factor in corrosion.

2.3 Temperature measurement by FBG

Knowing the importance of temperature measurement in the sensor, an alternative that can be coupled without suffering electromagnetic interference are the optical fiber sensors. Besides, especially because the low mass, the response of the optical fiber to thermal variations are very fast, making the measurement speed limitation with the electronics, not with the sensor. The use of optical fiber Bragg grating (FBG) are allowed to measurements of parameters such as load, vibration, strain and temperature and it have been widely extolled in the research literature (KERSEY et al., 1997). As cited by Rao (1999), the FBG sensors have been demonstrated for a number of applications measuring temperature, including for strain compensation, directly in electric power industry, medicine, chemistry and others. For this work these sensors were encapsulated in non-metallic materials, such as alumina (aluminum oxide - Al_2O_3). This material was chosen because of several characteristics such as high thermal conductivity around $30 \text{ W}/(\text{mK})$ according to Haynes (2016), which means low thermal inertia and fast measurements for temperature, chemically inert and does not interfere electrically with impedance sensors.

The FBG consists of a periodic change produced in the refractive index of the fiber core along its axis. The Bragg grating and the signal response (spectra) can be seen in Figure 21.

Figure 21 - Bragg grating and incident, reflected and transmitted spectra.



Source: Adapted from Schlüter (2010).

On reaching the broadband spectrum on an optical fiber containing a Bragg grating, the light reflects a fraction of the band occurs through the coherent scattering effect at the interfaces that separate the regions with different refractive index. According to Hill and Meltz (1997), the central wavelength of the reflection spectrum occurs close to the Bragg (λ_B) wavelength of the lattice, which satisfies the Bragg condition in the first order for normal incidence, which is given by:

$$\lambda_B = 2n_{eff}\Lambda, \quad (2.15)$$

where n_{eff} is the effective refractive index of propagation mode and Λ is the period of the grating.

The sensing capacity of the Bragg grating is directly related to the fact that λ_B can be altered by two independent modes: (i) Due to a mechanical effort that causes a change in the periodicity of the structure, Λ or (ii) due to temperature variations that result in the alteration of the refractive index n . This dependence can be described in an approximately linear fashion:

$$\frac{\Delta\lambda_B}{\lambda_B} = 9 \times 10^{-6} \Delta T + 0.78\gamma, \quad (2.16)$$

where: ΔT is the temperature variation, measured in °C and γ represents the mechanical deformation, γ is a dimensionless quantity (defined as: $\Delta l/l_0$). In equation (2.15), the numerical constants depend on the material that makes up the fiber. The thermal constant may show variations between fibers. Therefore, the existence of longitudinal mechanical stress or temperature variation on a Bragg grating causes, due to the photoelastic and thermo-optical effects, the displacement of the Bragg wavelength, described by the equation:

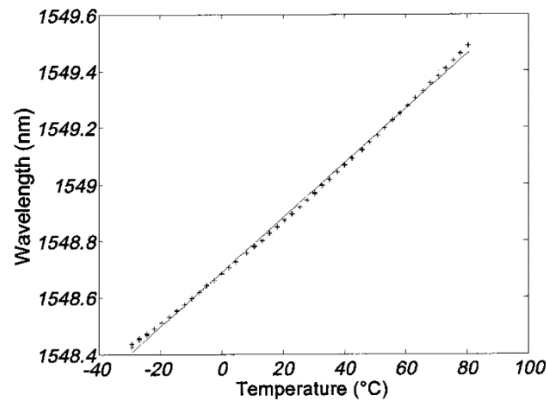
$$\Delta\lambda_B = 2 \left(\Lambda \frac{\partial n_{eff}}{\partial l} + n_{eff} \frac{\partial \Lambda}{\partial l} \right) \Delta l + 2 \left(\Lambda \frac{\partial n_{eff}}{\partial T} + n_{eff} \frac{\partial \Lambda}{\partial T} \right) \Delta T, \quad (2.17)$$

being: l is the length of the Bragg grating, T the temperature is ΔT the temperature variation. The variation of the Bragg wavelength ($\Delta\lambda_B$), described by equation (2.16), guarantees that the FBG sensor can be used as a sensor for strain or temperature. Sensing is effected by reading (in the optical domain of frequency) the position of the

center of the reflection band. According to Othonos (1997), by means of this information, the position of the Bragg wavelength, which represents the central position of the reflection band whose form is approximated by a Gaussian function.

To perform the FBG temperature characterization of temperature it is necessary to have a curve such as the one in Figure 22.

Figure 22 - Typical FBG temperature response.



Source: Adapted from Flockhart et al. (2004).

The specific calibration curve for our sensor can be found in section 3.2.1. with the temperature range, number of cycles, regression and calibration coefficient.

3. Sensor design, measuring systems and facilities

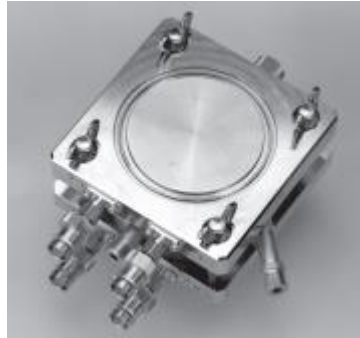
In this chapter the design and manufacturing process of the impedance sensors applied in this thesis are detailed as well as their application in different examples is given.

3.1 Overview

The electrical impedance sensors used for measurements in pipes are normally non-intrusive and formed by at least two electrodes. Such sensors have as main advantages the high temporal resolution and the low cost (FALCONE et al., 2009). According to Thorn et al. (2013), together with gamma ray, impedance sensors are the most commonly used in multiphase flow monitoring.

There are some commercial sensors that can be used for electrical impedance measurement. Among them, the sensor used for some measurements in this work was the Keysight 16452A liquid dielectric test fixture (Figure 23) allied to an impedance analyzer (Keysight 4294A, used frequencies from 40 Hz up to 5 MHz). This sensor provides impedance measurements of liquid materials employing the parallel plate method. More details on the experimental methodology can be found in Appendix A.

Figure 23 - 16452A Liquid dielectric test fixture.



Source: Keysight (2017).

Nonetheless, in order to facilitate the placement of a sensor in flow loops for hydrates monitoring, two new concave plate sensors were designed and built with the addition of FBG in one of them (for parallel temperature monitoring). The concave plates are copper electrodes and allow the acquisition of electrical impedance data of the substances.

For temperature measurements first we tried to use thermocouples as temperature probes, however, in addition to interfering with electrical measurements, they have a larger mass, also causing the response time to be longer than that of optical fiber. Furthermore, due to the knowledge already existing in the group for the manufacture and use of fiber, FBG was chosen as technique for temperature measurements.

3.2 Impedance sensors design and construction

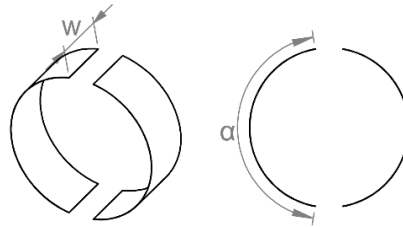
Several types of electrodes for impedance sensors have already been developed, as already mentioned (Section 2.1.7). However, in order to make a simple non-intrusive sensor that can be installed in pipes, the arrangement of concave plates was chosen.

3.2.1 Combined sensor

The concave plate electrodes (Figure 24) are basically two semi-cylindrical (half-rings) conductive plates placed around the duct in the measurement section facing each other. The greater the area of the sensor, the greater its sensitivity, and the closer to 180° the alpha angle, more intense the electric field in the region where the electrodes are close (STRAZZA et al., 2011). The width w can vary according to application and

available space and for the used sensor in this work, the dimensions will be shown later in Figure 25.

Figure 24 - Schematic representation and cross-section of the electrodes of concave plates.



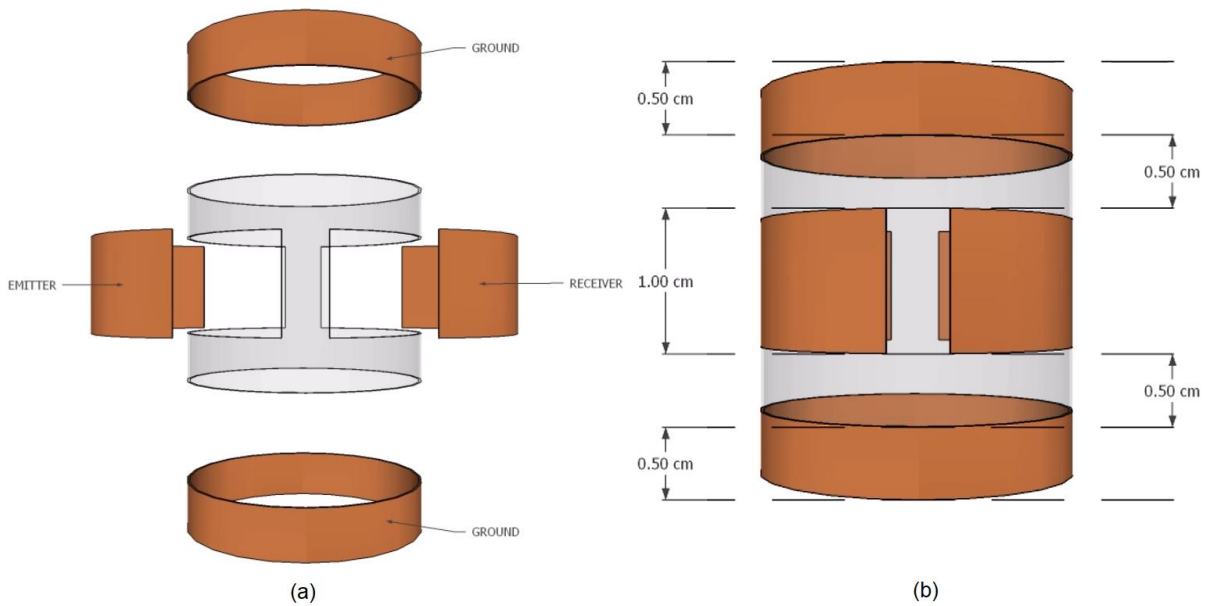
Source: Personal collection.

According to Elkow and Rezkallah (1996) it is worth noting that for any proposed electrode configuration, the sensor must be wrapped with a shielding conductor, in order to protect the sensor from external phenomena that may interfere with measurement. Such conductor must be grounded and be at a minimum distance from the measuring electrode to minimize changes in measurements. Also, two ground electrodes were placed around and the FBG makes measurements of temperature (Figure 25).

To ensure sufficient mechanical strength for the proposed application, the material used in the manufacture for hydrates sensor was fiberglass. In addition, this composite is versatile and widely used in industry. As main attributes of fiberglass composites, according to Wallenberger and Bingham (2010), are the mechanical and chemical properties such as lightweight, corrosion resistance, longevity and low cost.

The copper electrodes (copper tapes) are in direct contact with the test substance (inside the sensor) and the FBG used to measure temperature was encapsulated into a protective alumina tube. For this sensor we choose the copper tapes due to the ease of handling and possibility to shape it in the desired shape. Regarding the electrical cables, we choose one that has an outside mesh so that we could connect it to the external shield to avoid unwanted external interference. The electrical structure can be seen in Figure 25.

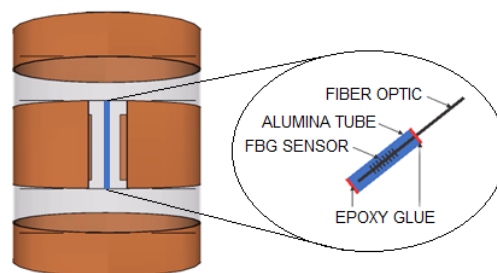
Figure 25 - (a) Exploded view of electrical structure of the concave plate sensor and (b) dimensions.



Source: Personal collection.

For the encapsulation process, we choose the alumina as explained in section 2.3 and the sensing part (with the Bragg grating) of the optical fiber was inserted into a alumina tube. This tube is larger than the sensing unit (6 cm) but the Bragg grating is kept in between the impedance emitter and receiver electrodes to make the local temperature measurements as close as possible to the place where the electrical measurements are made. The ends of the alumina tube are sealed with epoxy glue allowing the sensing part of the optical fiber to expand and contract only depending on the thermal variation, keeping it immune to load and strain variations. Figure 26 shows with more details the encapsulated FBG.

Figure 26 - Details of encapsulated FBG.



Source: Personal collection.

Using the commercial FEM (finite element method) simulation software COMSOL Multiphysics 5.0, the proposed geometry for electrical measurements was simulated to verify its capacitance behavior. The objective of the FEM is to make the discretization of a domain, making its representation by approximate means of a finite number of elements. Therefore, the method solves an associated problem (GIACCHINI, 2012).

The simulated capacitance of a point C_{sim} between the transmitter electrode and receiver electrode is calculated by integrating the induced surface charge density ρ over the electrode boundaries Γ

$$C_{sim} = \frac{1}{V} \int_{\Gamma} \rho(\Gamma) \cdot d\Gamma, \quad (3.1)$$

where the integral is implemented as post-processing option in the COMSOL Multiphysics 5.0 software. Using a physics-controlled mesh called extra fine was obtained an empty capacitance of 0.1 pF for concave plates, which is an acceptable capacitance value for the measurements to be performed.

The verification of this impedance sensor was performed using know substances such as air, mineral oil and water. Analyzing Table 3, which shows the simulated values and the measured values of capacitance, it can be concluded that the simulation is within the same order of magnitude of the measured values. Such differences are due to permittivity values used in simulations (for pure substances under certain temperature conditions) which are not always possible to reproduce accurately, and also to the slight differences in geometry caused by the manual process in the manufacture of the sensor.

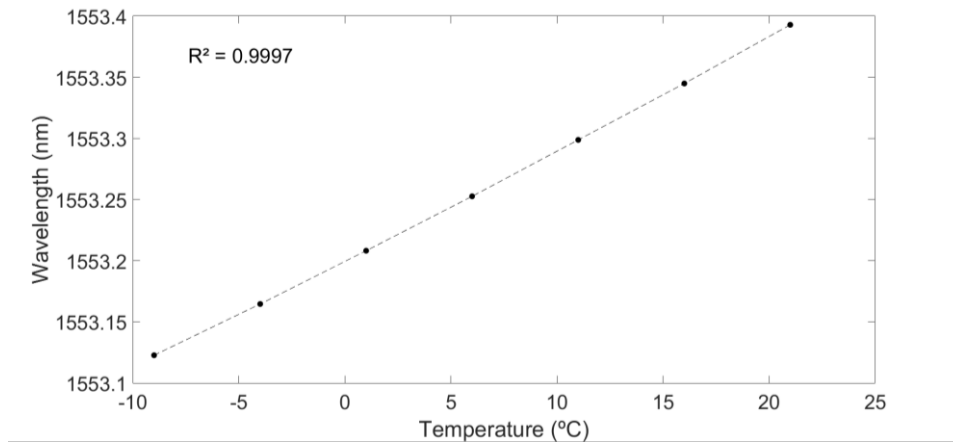
Table 3 - Simulates and measured values of capacitance for concave plate sensor.

	Simulation (F)	Measure (F)
Air	1.1 e^{-13}	2.9 e^{-13}
Mineral Oil	2.9 e^{-13}	3.1 e^{-13}
Water	8.6 e^{-12}	7.7 e^{-12}

Source: Personal collection.

A typical calibration curve for temperature measurements with the FBG was already showed in Figure 22 (page 50). However, we perform our specific FBG temperature response characterization using a LAUDA thermostatic bath and the sensor was introduced into the chiller and the temperature was varied from -9 °C to 21 °C. Seven repeat ups and downs were performed during the calibration experiment. The data showed a good linear fit, with $R^2 = 0.9997$, with a calibration coefficient of 0.009 nm/°C. The mean value of the measurements can be observed in Figure 27. The complete sensor with electrical, optical and fiberglass structure is illustrated in Figure 28.

Figure 27 - Temperature FBG calibration.



Source: Personal collection.

Figure 28 - Complete structure of sensor.

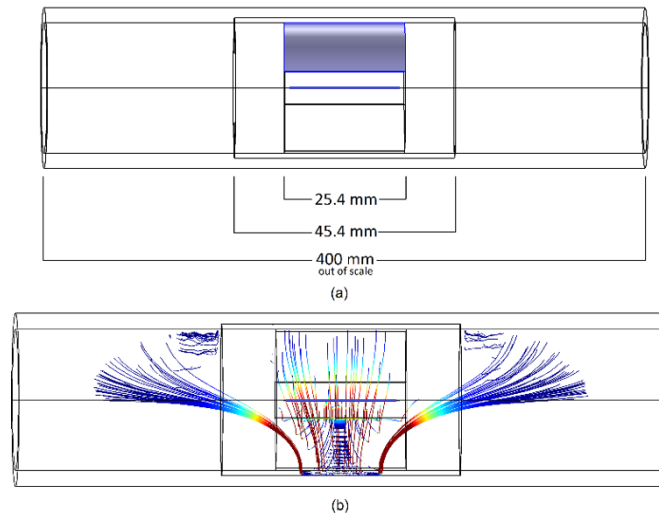


Source: Personal collection.

3.2.2 Deadleg sensor

With the aim of applying a sensor in the deadleg, the concave plate geometry was adapted according to Figure 29 and it will be called deadleg sensor.

Figure 29 - (a) new dimensions for the concave plate sensor (deadleg sensor) and (b) electric field behavior.



Source: Personal collection.

Now adapting the electrodes from sensor 1 for better coverage of electric field and for proper fitting inside the deadleg, the above measures were used (Figure 29). Although some electric field lines leave the area between the emitter and receiver electrodes in this geometry, the intensity of this field is not significantly large to interfere with the results. That is, such field lines do not have the intensity to measure phenomena or interferences external to the emitter and receiver electrodes.

Unlike the first model of concave plate sensor, as this would be used inside a metal pipe that could be used as ground, it does not have ground electrodes and was manufactured inside a piece of 1 inch PVC pipe. To make the electrodes more robust in this design, they were made of copper plates instead of using only the tapes, which made the mechanical composition stronger. The finished sensor can be seen in Figure 30.

Figure 30 - Concave plate sensor for deadleg.



Source: Personal collection.

Due to the small thickness of the sensor (less than 1 mm), it was designed to slide into the deadleg and, through a feedthrough, to have the electrical cables removed for connection to the measuring electronics.

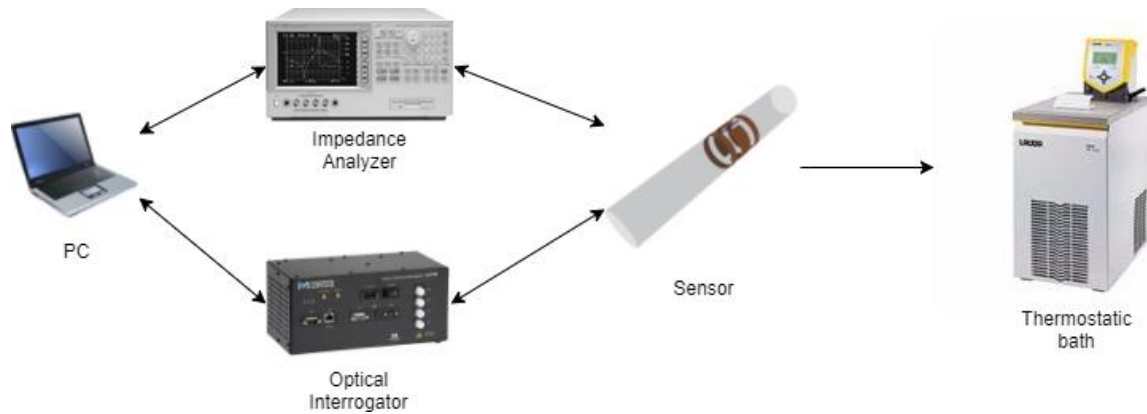
3.3 Acquisition systems and facilities

Some acquisition systems and facilities were used depending on the used sensor and also due to the type of desired data. One of the facilities are located in the Multiphase Flow Research Center at Federal University of Technology – Paraná in the city of Curitiba at campus Ecoville. And the other, with the purpose of acquiring more specific knowledge about hydrates and using the deadleg during the period of exchange, as exploratory experiments, laboratories were used in Colorado School of Mines (CSM) at Chemical and Biological Engineering Department.

3.3.1 Multiphase Flow Research Center (NUEM) facility

To test the sensors, we used some systems to do data acquisition and thermal conditioning. For temperature control of ice and hydrates formation a chiller from LAUDA was used. For optical and impedance data acquisition we used the proper software and a diagram of the system for concave plates sensor is shown in Figure 31.

Figure 31 - System diagram for concave plates sensor.



Source: Personal collection.

The precision impedance analyzer (Keysight 4294A) is connected to a computer and to the sensor, as well as the optical interrogator. With this commercial system is possible to perform a logarithmic frequency sweep from 40 Hz to 5 MHz. A full scan lasts about 9 seconds and it was repeated every 5 minutes and to connect the impedance analyzer to computer a USB/GPIB interface was used. We choose the parallel equivalent circuit model in the equipment using as a guideline the high and low impedance criteria (Keysight, 2016b) which can be used to roughly discriminate the frequency range. Because of that our measurements will be in the parallel mode (C_p and R_p). The basic measurement uncertainty for impedance measurement is $\pm 0.08\%$ (Agilent, 2008).

Technically, the impedance analyzer can operate in a frequency range from 40 Hz to 110 MHz (1 mHz resolution), however, according to the manufacturer, for frequencies higher than 5 MHz a cumbersome calibration method (AGILENT, 2003) is required and therefore upper frequency is limited to 5 MHz. The equipment employs the auto-balancing-bridge technique for our measurements, in which a current signal is inserted and a voltage signal is read and have as main advantage the high accuracy. Also, the four-terminal-pair (4TP) is used because that configuration can reduce the effects of lead impedances and contact resistances since the signal current path and voltage sensing leads are independent.

The sensor is placed inside the chiller, within a mixture of mono ethylene glycol and water. This mixture allows temperatures below $0\text{ }^{\circ}\text{C}$ without it freezing. Thus, it is possible to freeze water or form hydrates inside the sensor without the worry of the freezing chiller liquid.

The calibrations for the cable length correction is always performed and the open/short compensation is performed for the commercial sensor (Keysight 16452A liquid dielectric test fixture) as mentioned in Appendix A, where an operating manual for conducting such tests has been written.

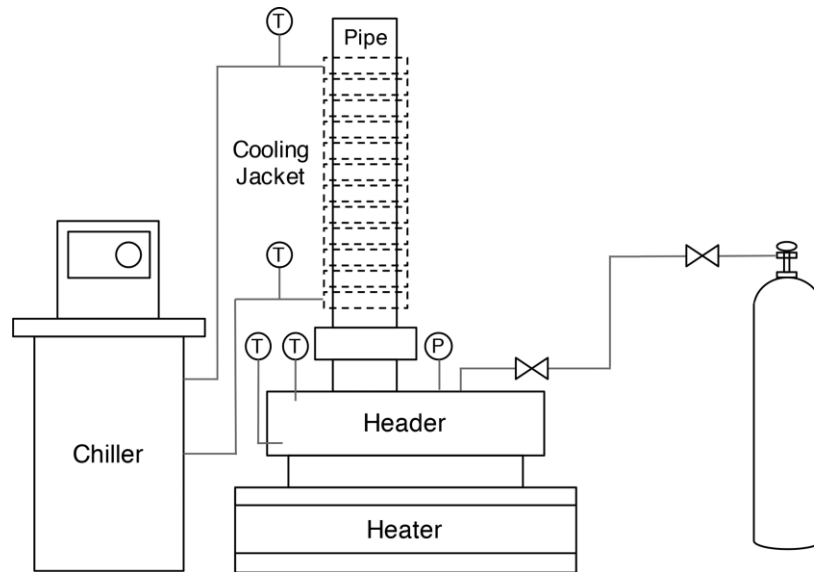
Regarding the optical interrogator, the equipment is the SM130 from Micron Optics, it is a 4 input channel, 1 kHz acquisition rate, wavelength stability $\Delta\lambda = 2$ pm and wavelength repeatability $\Delta\lambda = 1$ pm.

3.3.2 Deadleg facility at Colorado School of Mines (CSM)

Although the group had deadlegs with different diameters and lengths, the one chosen for the tests was the vertical stainless steel pipe of 49 cm of length and 1-inch inner diameter. The smaller was chosen for the first tests since the hydrate formation in larger deadlegs may take months, while in the lower this time is of days or maximum weeks and also have a simpler operation compared to larger ones.

This experimental apparatus (Figure 32) is designed to mimic the deadlegs in oil and gas industry and can support high pressures (up to 150 bar). The pipe volume is 255 ml and is wrapped with copper coils to control the pipe wall temperature. On the top of the pipe was attached a feedthrough from Swagelok to remove the sensor wires from the pipe. It was assembled with a 300 ml header bellow the pipe, so it was possible to control the temperature and the mixing rate of the magnetic stirrer placed inside the header. A gas line can be connected to the apparatus for gas injection and pressurization and it is possible to monitor temperature and pressure with commercial sensors by LabVIEW.

Figure 32 - Deadleg system for hydrate studies.



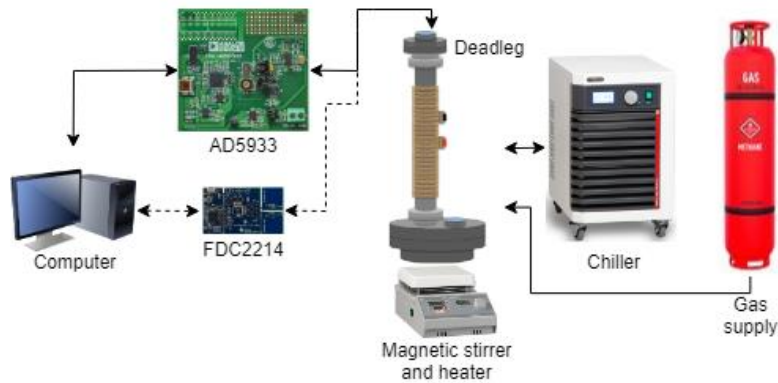
Source: Sa et al. (2017).

For data acquisition two different systems were used. The first one was the AD5933 evaluation board, which is a high precision impedance converter system that combines an on-board frequency generator with a 12-bit analog-to-digital converter. With an accuracy of 0.5% and an impedance measurement range from 1 k Ω to 10 M Ω . However, we operate this system from 10 kHz to 100 kHz, a more recommended frequency for this sensor design. Using the proprietary evaluation software (downloadable at Analog Device) and with the help of a macro to make the acquisitions in the desired time interval (also 5 minutes) and save the results, after performed the calibrations, the system is ready to measure.

The last system was the FDC2214, which enables the capacitance measurements with high resolution (up to 28 bits) and can detect very small variations (for our case, in the order of fF). Regarding the Texas Instruments electronics, it is a multi-channel electronics, noise and electromagnetic interference resistant, with high resolution and high speed capacitance to digital converter. The excitation frequency is from 10 kHz to 10 MHz and depends of the substance in analysis, since it is a parallel LC resonant circuit also in parallel with the unknown capacitance of interest.

A schematic overview is shown in Figure 33.

Figure 33 - Schematic overview of CSM facilities.



Source: Personal collection.

For this system, the computer can control the electronics connected with the sensor, but as there is only one concave plate sensor available, it is necessary to choose only one electronics to operate at a given time (AD5933 or FDC2214). The sensor is inserted into the 1-inch deadleg and the already described system is ready to operate.

3.4 Matlab algorithm

As already mentioned in section 2.1.4 the used method to fit the data is the nonlinear least square fitting and the used function in Matlab R2016a is the “lsqcurvefit” which solves nonlinear least square problems. The standard algorithm of this function is the trust region reflective and it starts at a given initial value for all variables (or parameters), so we need to give a first guess before run the script.

However, first we insert the inputs, such as our frequencies (xdata) and impedances (ydata). It is necessary to split impedance data into real and imaginary due to a need of parameters restriction. As mentioned, we restricted the parameters in lower and upper bounds, since the function can return physically inexplicable values such as negative resistances. Knowing the equivalent electrical circuit model (mentioned in section 2.1.5) we have 8 parameters: R_1 , τ_1 , R_2 , τ_2 , R_3 , τ_3 , n_3 and τ_4 . Except for n_3 which is in between 0 and 1, the parameters are restricted in a range from 0 to infinite, so that the solution is in the range lower bounds < solution < upper bounds

Given the initial values, the algorithm finds the best fit for our data regarding the model that we insert (Figure 6). When the function converges to a solution it will stop and we have the 8 parameters.

4. Tests and results

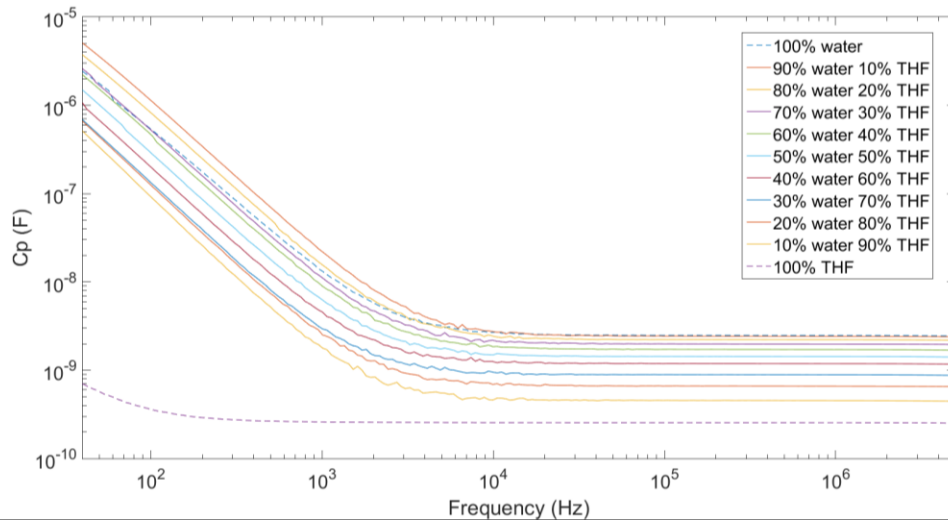
Initially some validation experiments were performed and due to the similarities between ice and hydrates, the preliminary experiments were given by freezing deionized water inside the sensor. Using the data of temperature, capacitance and resistance obtained, some graphs have been plotted and can illustrate with more clarity what the sensor detects. After that, hydrates formation was performed and results are shown. We performed all experiments at least three times to ensure repeatability.

4.1 Verification experiments

Aiming the objectives cited at the beginning of this document, with a focus on developing sensor for hydrates formation detection, some validation experiments were performed.

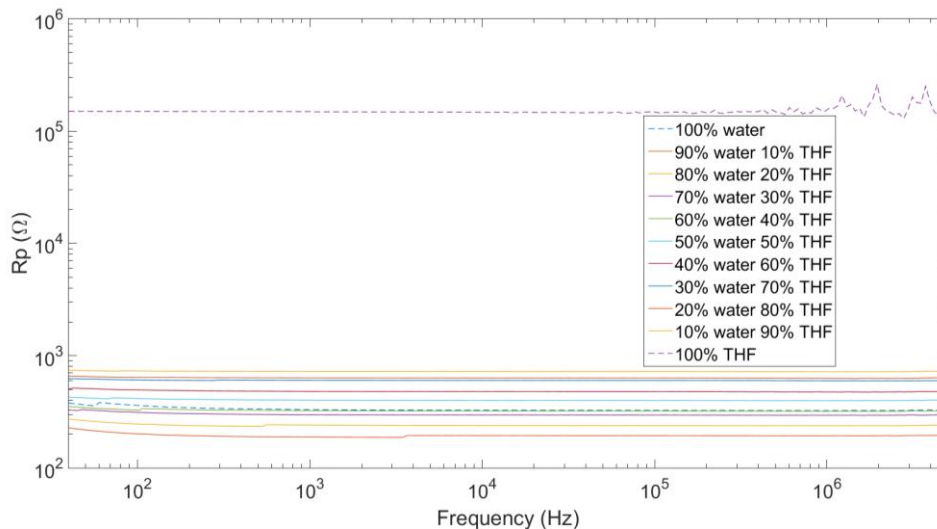
With the purpose of analyzing the system response to different concentrations in mixtures, not only with pure substances, we performed an experiment by mixing THF, a substance of interest, with deionized water in different proportions using a commercial sensor (resistant to corrosion caused by the used organic compound), and the measured spectra are in Figure 34 and Figure 35.

Figure 34 - Frequency versus capacitance of THF and deionized water mixture.



Source: Personal collection.

Figure 35 - Frequency versus resistance of THF and deionized water mixture.

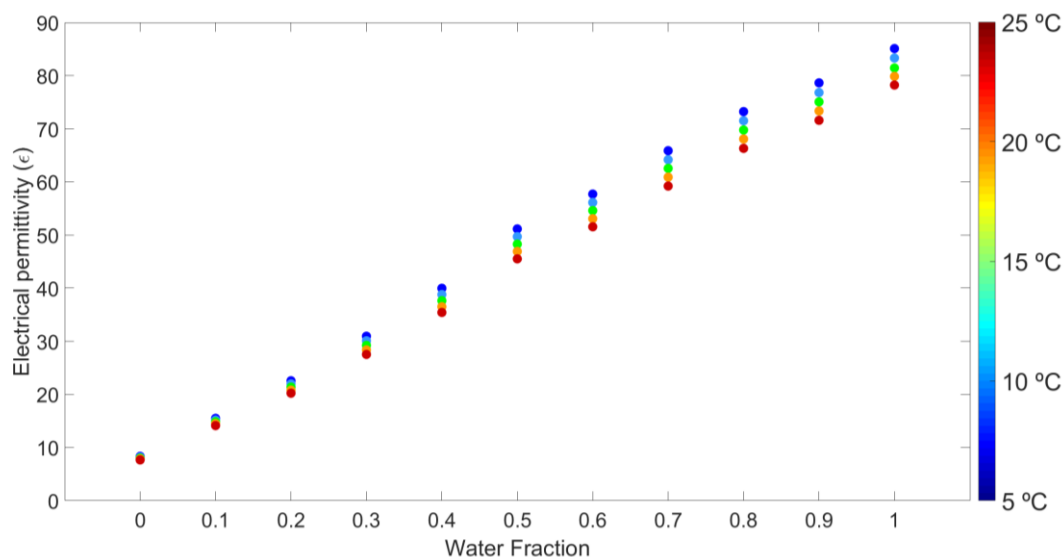


Source: Personal collection.

The water influence in the mixtures are strong. Knowing the great discrepancy between water and THF permittivity values (78 and 7.52 respectively) it is clear that a minimum amount of water can shift the capacitance spectra up and resistance spectra down. Another different behavior between water and THF is the low frequencies capacitance behavior (up to 10 kHz) where the spectra of pure water is in the middle of the mixtures spectra.

In addition, the mixtures were injected into the commercial cell that was inserted into the chiller for temperature control. After the thermal stabilization the measurement was performed and the data processed for 5 different temperatures, which are shown in Figure 36. Due to double layer capacitance effect, the low frequency permittivity values were discarded and only left the values for a fixed frequency (5 MHz). Pure THF was initially measured and then we prepare and measure mixtures with different THF and water concentrations (from 100% THF increasing the deionized water fraction by 10% until we have only pure deionized water). The chart does not represent values for air, however it remains with the permittivity always close to 1, consistent with the literature (Haynes, 2016). Pure THF kept the values from 7.6 to 8.3 and water between 78.1 and 85, as the temperature was lowered, in agreement with the values already shown in Table 1. And regarding the mixtures of THF and water, for the value quoted in the cited table (20% THF and 80% water) the measurements were, according to the decrease in temperature, from 66.3 to 73.3, consistent with Collie et al. (1948) where the water permittivity decreases with the increasing temperature, in view of the water dominance permittivity values as observed in Figure 34 and Figure 35.

Figure 36 – Static permittivity for THF and water mixtures using commercial cell. Permittivity was evaluated at 5 MHz.



Source: Personal collection.

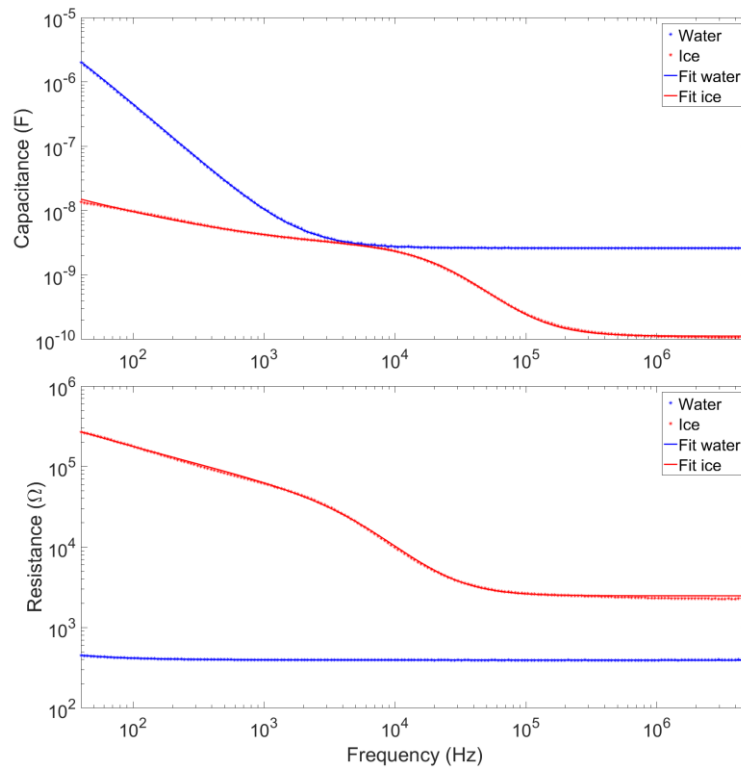
Having measured these two known substances, ensuring the repeatability of sensor results, measured the mixtures of different proportions of THF with deionized

water in some temperatures and thus having reference values, it was possible to initiate the ice-forming experiments.

4.2 Ice formation monitoring using the commercial sensor

After system calibration and evaluation, the ice formation experiments were performed. The commercial sensor has the advantages of easy calibration, non-interference by external noise, mechanical robustness and easier data equation. Thus, deionized water was inserted into the cell which was cooled to $-10\text{ }^{\circ}\text{C}$ until complete solidification. We obtained the data using the impedance analyzer and the result is plotted in Figure 37.

Figure 37 - Capacitance and resistance Bode plots for ice formation fitted with $R||C + C||(R + R||Q)$ using the commercial sensor.



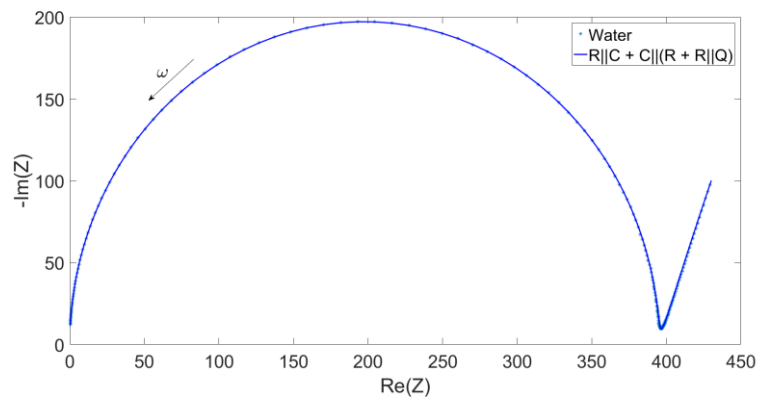
Source: Personal collection.

Using then the constant phase element, some equivalent circuits were tested and the best one, able to fit any experiment with a good agreement, is the already presented in Figure 6. So, all fits were performed using the already presented equivalent electrical circuit model (Randles circuit – section 2.1.5). We chose this circuit because it can be

adapted with a good agreement for all our data (from pure water and THF to ice and hydrates).

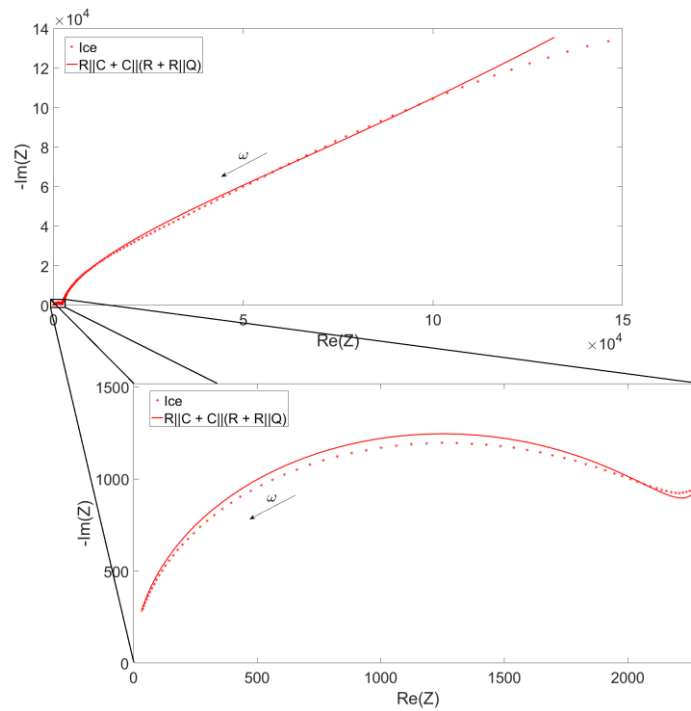
Converting the data to impedance and fitting it again with the selected equivalent circuit we have the following graphs for water (Figure 38) and ice (Figure 39). In this type of plots, the frequency increase to the left, as indicated by the ω arrow.

Figure 38 - Water impedance fitted with $R||C + C||(R + R||Q)$ using the commercial sensor.



Source: Personal collection.

For the ice impedance a zoom in is also plotted in order to observe the highest frequency behavior and how the model fits the data.

Figure 39 - Ice impedance fitted with $R||C + C||(R + R||Q)$ using the commercial sensor.

Source: Personal collection.

The eight parameters from the already mentioned equation (section 2.1.5) can be written in Table 4 for water and ice fits.

Table 4 - Parameters obtained from fitting impedance data for water and ice for the commercial sensor.

Parameters	Water	Ice
R_1 (Ω)	1.78e04	2.30e03
τ_1 (s)	3.80e01	2.70e-07
R_2 (Ω)	3.96e02	9.82e06
τ_2 (s)	1.04e-06	2.81e-02
R_3 (Ω)	4.56e03	36.26e02
τ_3 (s)	4.54e-01	1.16e-01
n_3	0.80	0.61
τ_4 (s)	1.43e-04	1.55

Source: Personal collection.

The main differences between water and ice parameters are the time constants τ . Analyzing them it is possible to distinguish the physical state of the substance and we also have realistic values for the resistances. Thus, the equivalent circuit can be validated for this experiment and is able to fit the liquid and the solid state for separated capacitance and resistance data and also for the combined impedance data.

4.3 Ice formation monitoring using the combined sensor

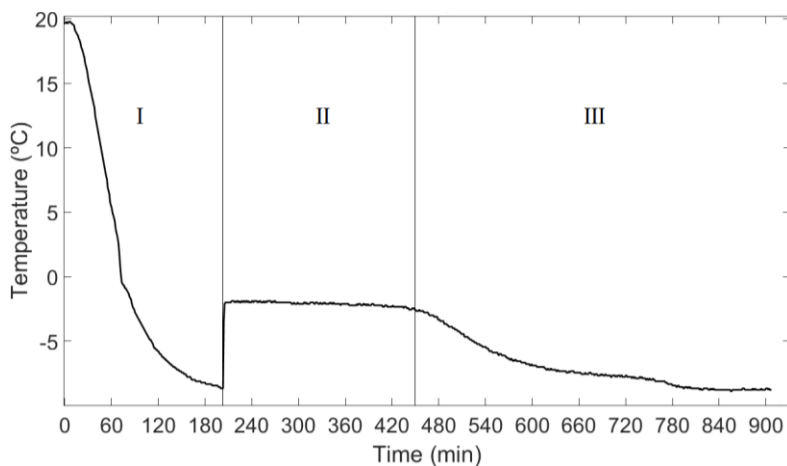
With the purpose of freezing deionized water inside the combined sensor, we placed it inside the chiller with a setup temperature of $-9\text{ }^{\circ}\text{C}$ and the initial temperature was room temperature (about $20\text{ }^{\circ}\text{C}$). The experiment start and the temperature is lowered until the chiller reaches $-9\text{ }^{\circ}\text{C}$. As the thermal inertia of the sensor is relatively large, it takes a while until the temperature FBG reaches the chiller temperature.

The results will be divided in two parts. First the temperature behavior will be analyzed and then the electrical impedance. For the electrical impedance, we will have more plots since this sensor was totally manufactured in our lab and the geometry is closer to the desired one for real application. Besides, the temperature measurement inside the sensor is only possible with the combined sensor.

4.3.1 Temperature

A very important part of the analysis of such experiments is to understand the behavior of temperature inside the sensor. For this, the encapsulated FBG monitored this variable. In Figure 40 it is possible to observe a graph of time versus temperature.

Figure 40 - Temperature behavior during ice formation.



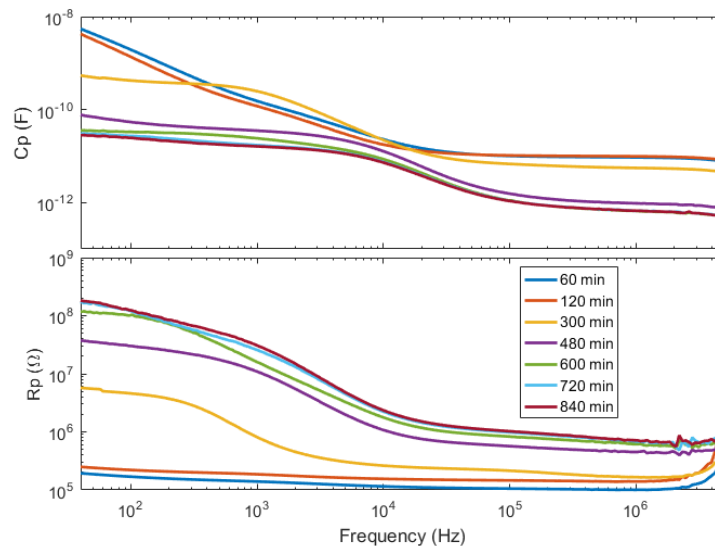
Source: Personal collection.

Analyzing the ice formation graph, a normal behavior for this substance is seen. At region I there is progressive cooling, where the temperature falls below zero, but there is no change in physical state. At this moment we have the supercooling state, a metastable state, that is, we technically already have the temperature and pressure conditions to change physical state, however the substance remains in a state not consistent with the conditions. When the nucleation process began, the super cooled water changes its physical state, becoming solid and forming ice. As we can see, this is a fast phenomenon (as explained in section 2.2.2). After that, in section II of the graph, the ice losses its latent heat until the chiller extracts all possible heat at section III and temperature stabilize in $-9\text{ }^{\circ}\text{C}$.

4.3.2 Electrical impedance

Along temperature monitoring, electrical capacitance and resistance were monitored. We can see the spectra in Figure 41.

Figure 41 - Frequency versus capacitance and resistance spectra during ice formation experiment.



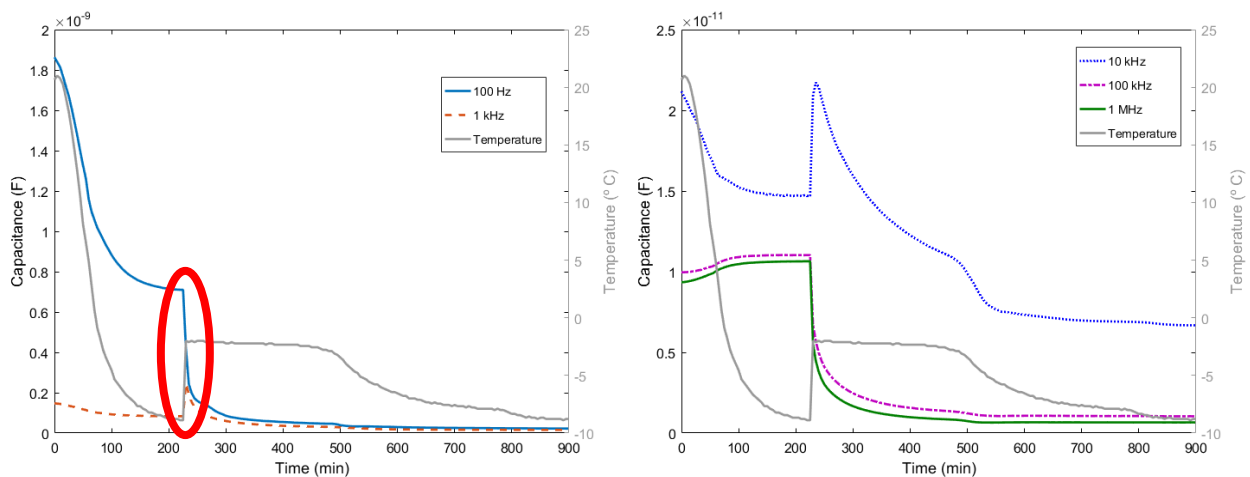
Source: Personal collection.

It is possible to detect changing in physical state of substances using electrical impedance spectroscopy, as we can observe in both spectra: liquid water until 120 min of experiment and solid water (ice) from 300 min. From 2 hours to 3 hours we can observe a significant change in capacitance and resistance spectra, especially for lower frequencies (up to 10 kHz), being this the solidification point for deionized water in

this experiment. We observe that even after the water solidification, the capacitance and resistance values continue to change during the experiment (decrease and increase, respectively), due to thermal stabilization. We did not observe a significant change in spectrum and other relaxation process during this process due to the change of physical state until the end of the experiment. However, there are numerous kinds of ice (Figure 17), and if the temperature drops to other levels and we increase the pressure, we would probably notice a new change in spectrum, due to the change in the ice structure formed. Another fact observed is the greater electrical conductivity in liquid medium, since the electrical resistance of ice is always greater than that of liquid water. All of these observations can be extrapolated to the other experiments present in this thesis involving changing the physical state of substances.

Moreover, to better visualize the capacitance and resistance behavior during water solidification, another plot was made. Five frequencies (100 Hz, 1 kHz, 10 kHz, 100 kHz and 1 MHz) were chosen and in Figure 42 it is possible to observe the capacitance spectra behavior along time and compare with temperature. By scale, the graphs were divided into two and in the first one we have highlighted the main event, which can also be visualized at the same point in the other graphs of the same experiment.

Figure 42 - Capacitance spectra for ice for 100 Hz, 1 kHz, 10 kHz 100 kHz and 1 MHz compared with temperature.

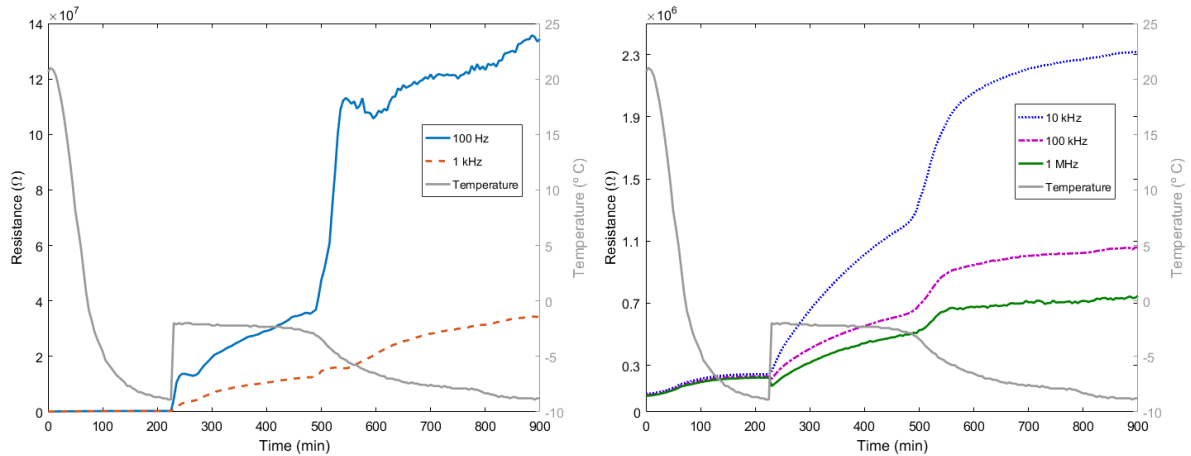


Source: Personal collection.

Thus, the behavior of electric capacitance at the moment of the physical state change is abrupt for the different frequencies studied and makes clear the relation

between the capacitance and the nucleation of the water. Also, in the same way, resistance spectra is shown in Figure 43 for the same frequencies.

Figure 43 - Resistance spectra for ice for 100 Hz, 1 kHz, 10 kHz, 100 kHz and 1 MHz compared with temperature.

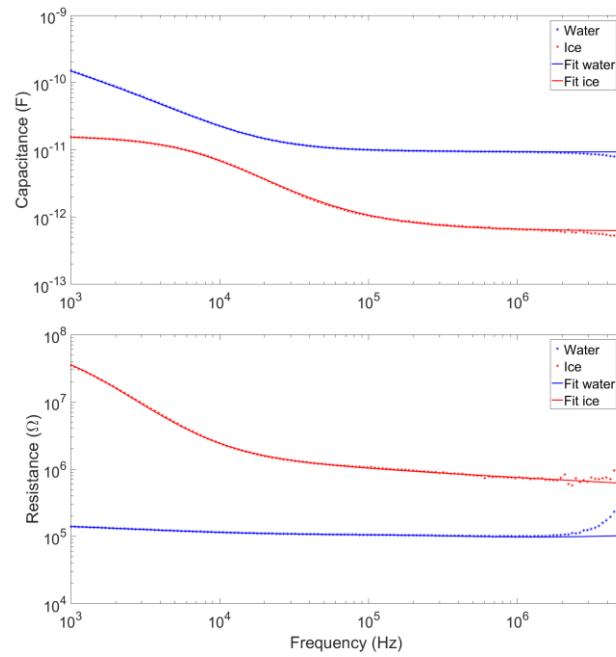


Source: Personal collection.

As well as the capacitance, the resistance shows a good predictor of physical state change, including being better at detecting section III of the temperature graph (Figure 40), being able to detect in a more precise way the moment in which the substance under analysis loses its latent heat and has its temperature equal to that of the external environment.

Applying the model only for the first and last curves, restricting the frequency from 1 kHz to 5 MHz for a better fitting, we have the Figure 44 for capacitance and resistance.

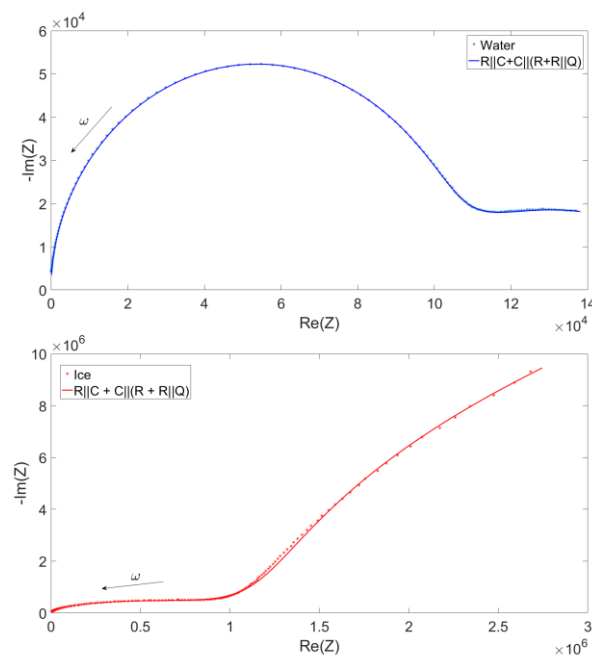
Figure 44 - Capacitance and resistance Bode plots for ice formation fitted with $R||C + C||(R + R||Q)$ using the combined sensor.



Source: Personal collection.

Converting the data to impedance and fitting, we have Figure 45 for water and ice.

Figure 45 - Water and ice impedance fitted with $R||C + C||(R + R||Q)$ using the combined sensor.



Source: Personal collection.

The equation parameters for the equivalent electrical circuit cited in section 2.1.5 can be summarized in a Table 5:

Table 5 - Parameters obtained from fitting impedance data for water and ice for the combined sensor.

Parameters	Water	Ice
R_1 (Ω)	9.36e04	6.85e07
τ_1 (s)	1.03e-06	1.17e-03
R_2 (Ω)	5.74e03	8.94e07
τ_2 (s)	3.75e-07	5.75e-05
R_3 (Ω)	7.33e04	1.28e07
τ_3 (s)	1.30e-04	4.16e-03
n_3	0.56	0.88
τ_4 (s)	2.77e-06	0.16

Source: Personal collection.

For water we can see that the tail occurring for low frequencies is represented by the second layer of the equivalent electrical circuit (Figure 6), the adapted part of Randles circuit, while the circular arc at high frequencies is modeled by the $R||C$ element. However, for ice it is vice versa. Hence, always the more dominant part of the plot is modeled by the $R||C$ circuit during ice formation.

All these observations are possible specially in order to molecular differences between liquid water and ice. In liquid water the molecules are connected by hydrogen bonds and are free to move, making the fluid amorphous. In ice the particles are in a fixed lattice arrangement, however, in order to line up the molecules, they need to be in rather open arrangement, giving a low density to ice and thus it is possible to detect the differences in the substances when under electric field effect.

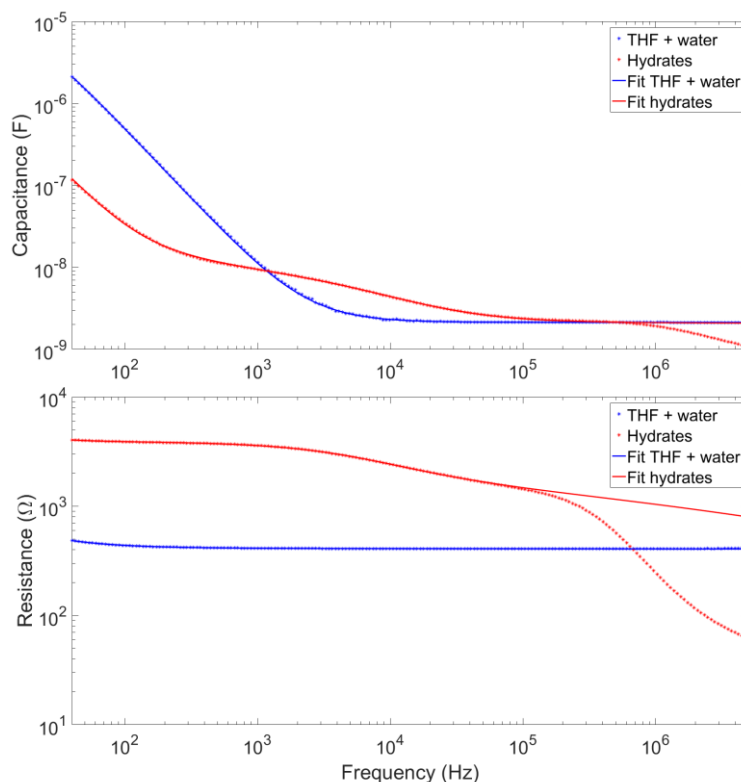
4.4 Hydrates formation using the commercial sensor

With the advantages already mentioned of the commercial sensor, now the hydrate experiments were performed. A mixture of deionized water and THF was prepared using a concentration, by weight, of 81% water and 19% tetrahydrofuran, being this the balance in hydrate formation so that there is no free THF or water after solidification. Since we are operating in a temperature range that would make it

possible for ice to form, one concern was whether what we were measuring was really hydrate or ice. However, the ice spectrum is very different from hydrates spectrum because the hydrate formation is privileged since the mixture is in stoichiometric proportion and the hydrate cages start to form from 4 °C, while for ice the required temperature would be at least 0 °C in the ambient pressure conditions. So, if we have accidentally a small percentage of ice, it will not influence the main goal of this work. Knowing that, the following experiments can be performed in a temperature under 0 °C, once hydrates may form faster than ice. Furthermore, a study by Barrer and Ruzika (1962) suggest that is possible to form hydrates (sI and sII) from ice in a nonagitated chamber at temperatures below the ice point.

Choosing an operation temperature of -10 °C, the experiments were performed and the capacitance and resistance response are plotted in Figure 46.

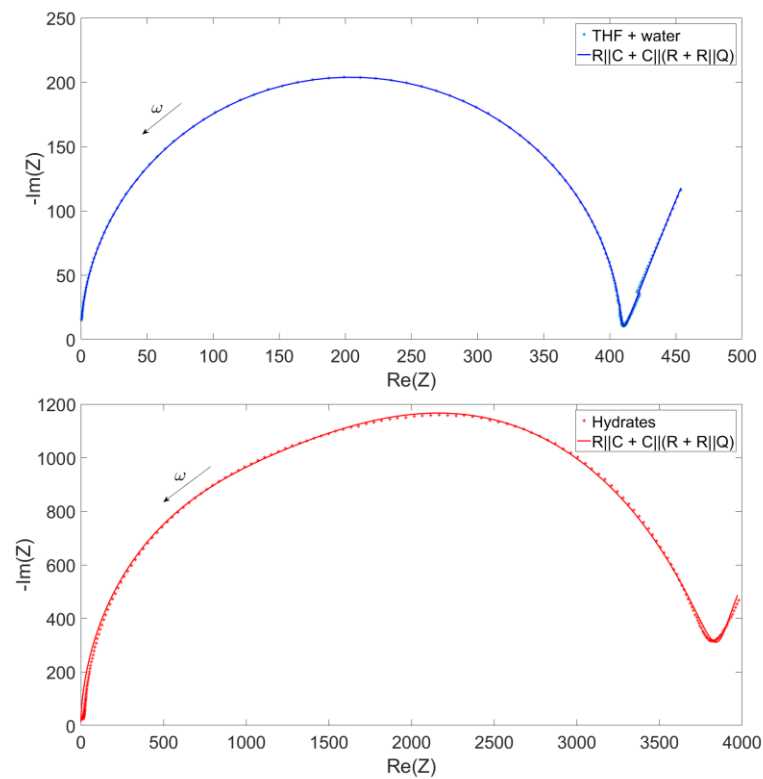
Figure 46 - Capacitance and resistance Bode plots for hydrates formation fitted with $R||C + C||(R + R||Q)$ using the commercial sensor.



Source: Personal collection.

A very different spectrum between the solid and liquid mixture was observed, indicating that the system is able to detect the solidification. Regarding to the fit, we can observe a good agreement for the THF plus water mixture, however for hydrates the good agreement is only up to 1 MHz to capacitance and 100 kHz to resistance. The plots indicate that the proposed model can fit most of the frequency range for the experiment. Hence, when the data is converted to impedance and the model is applied, it seems to have a better fitting, even in the higher frequencies (Figure 47).

Figure 47 - THF + water and hydrates impedance fitted with $R||C + C||(R + R||Q)$ using the commercial sensor.



Source: Personal collection.

Table 6 brings the parameters values:

Table 6 - Parameters obtained from fitting impedance data for THF + water mixture and hydrates for the commercial sensor.

Parameters	THF + water	Hydrates
R_1 (Ω)	1.75e04	1.94e03
τ_1 (s)	6.12e02	1.78e-02
R_2 (Ω)	4.10e02	2.03e03
τ_2 (s)	8.73e-07	4.21e-06
R_3 (Ω)	4.58e03	1.88e03
τ_3 (s)	3.81e-01	3.65e-05
n_3	0.79	0.71
τ_4 (s)	1.44e-04	1.25e-05

Source: Personal collection.

Mainly considering the desire to use a single equation that allows the fit of all experimental ice and hydrates data, regardless of the sensor used, the selected model presents a satisfactory fit even in the case of high frequencies for hydrates in this experiment.

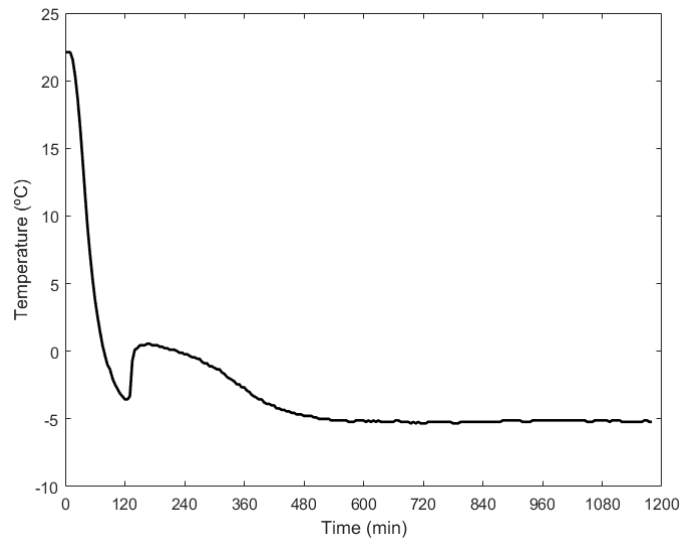
4.5 Hydrates formation using the combined sensor

A mixture of THF and water with a total volume of 60 ml were placed inside the sensor and it was sealed because the substance is volatile. The sensor was cooled down until -5 °C and data were monitored.

4.5.1 Temperature

The temperature of THF + water mixture was monitored while it was cooled down and can be observed in Figure 48, being similar to ice formation.

Figure 48 - Temperature behavior during hydrate formation. Chiller set point was $-5\text{ }^{\circ}\text{C}$.



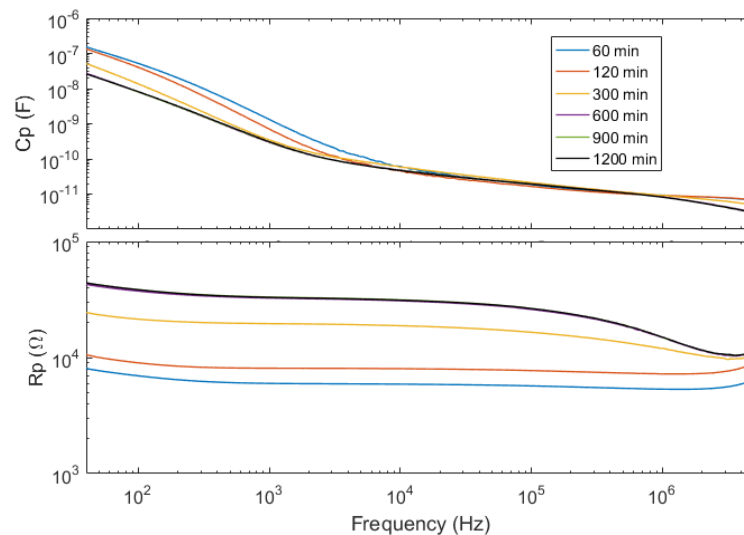
Source: Personal collection.

For hydrates, the behavior of temperature can be compared to ice formation, because the three phases already mentioned for ice (4.3.1) can be observed also here. The difference in the formation of the two substances is that ice has a more instantaneous formation when compared to hydrates.

4.5.2 Electrical impedance

As in ice, electrical capacitance and resistance values were monitored by scanning the frequency spectrum. For the formation of hydrates, the spectra are in the Figure 49.

Figure 49 - Frequency versus capacitance and resistance spectra during hydrate formation experiment.

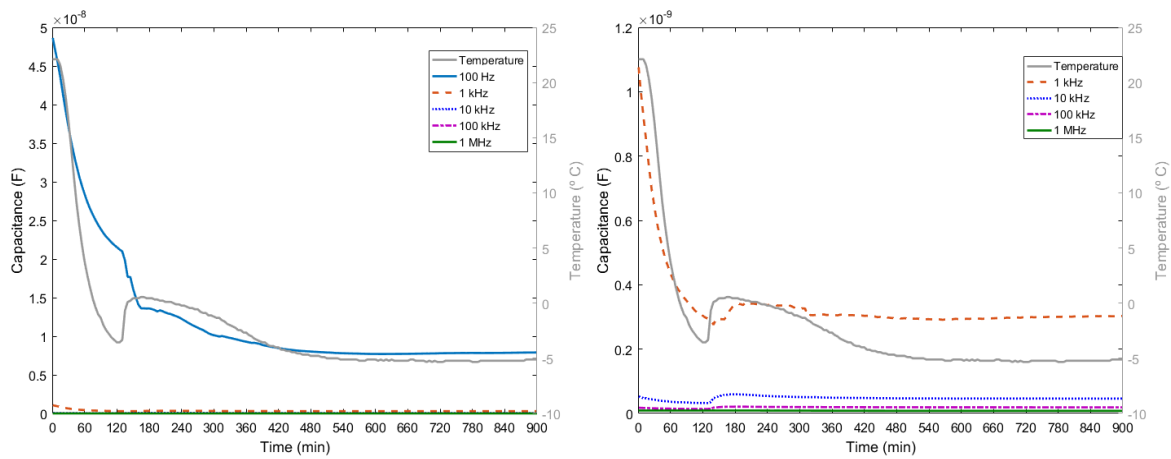


Source: Personal collection.

For this experiment, the capacitance spectrum had a slight change in the liquid to solid mixture. On the other hand, by analyzing the resistance spectrum, the change becomes more evident when the solidification of the mixture occurs, from 120 minutes to 300 minutes of experiment.

As well as for ice, the same frequencies were separated, one every decade, and their behaviors over time were plotted together with the temperature, according to Figure 50 and Figure 51 for capacitance and Figure 52 for resistance.

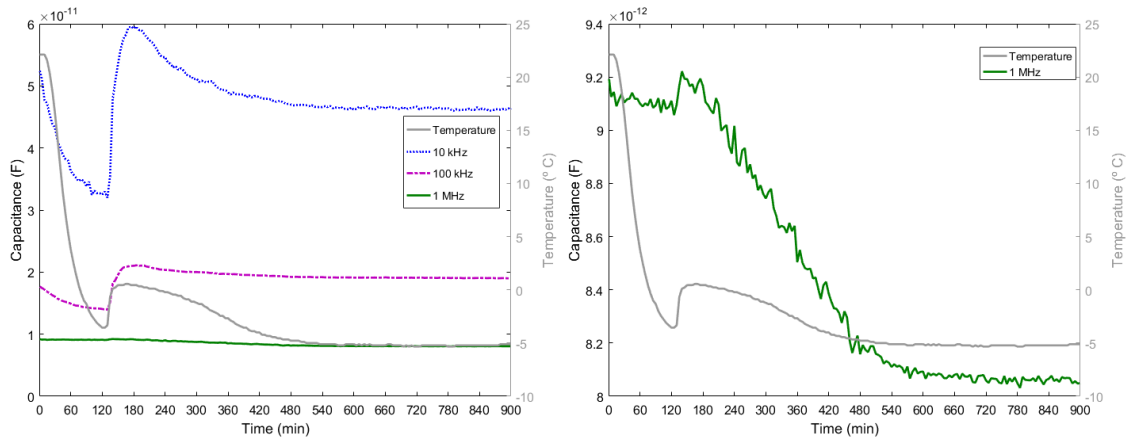
Figure 50 - Capacitance spectra of hydrate for 100 Hz and 1 kHz compared with temperature.



Source: Personal collection.

As there is a scale problem for viewing all selected frequencies, the following graphs were generated.

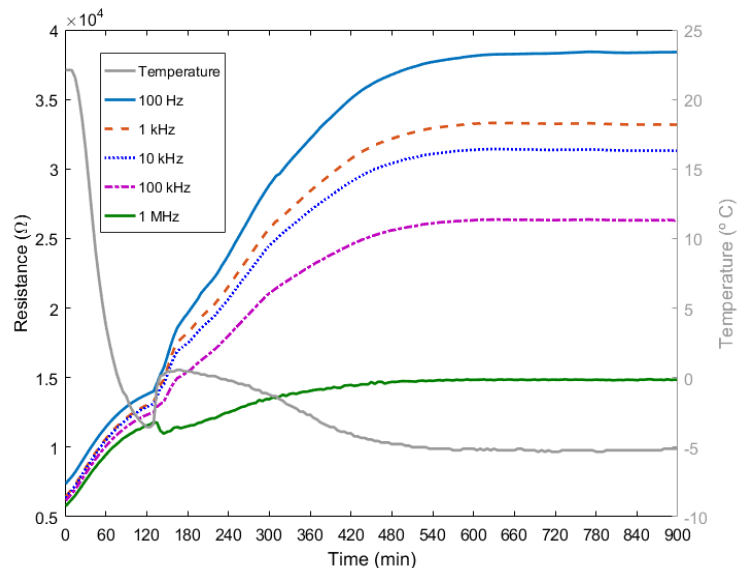
Figure 51 - Capacitance spectra of hydrate for 10 kHz, 100 kHz and 1 MHz compared with temperature.



Source: Personal collection.

As expected, similarly to the ice response, the capacitance responds to the solidification process of the mixture and has a significant change in its absolute values when the physical state changes. After approximately 120 minutes of the beginning of the experiment is observed the variation in capacitance values for all frequencies.

Figure 52 - Resistance spectra for ice for 100 Hz, 1 kHz, 10 kHz, 100 kHz and 1 MHz compared with temperature.



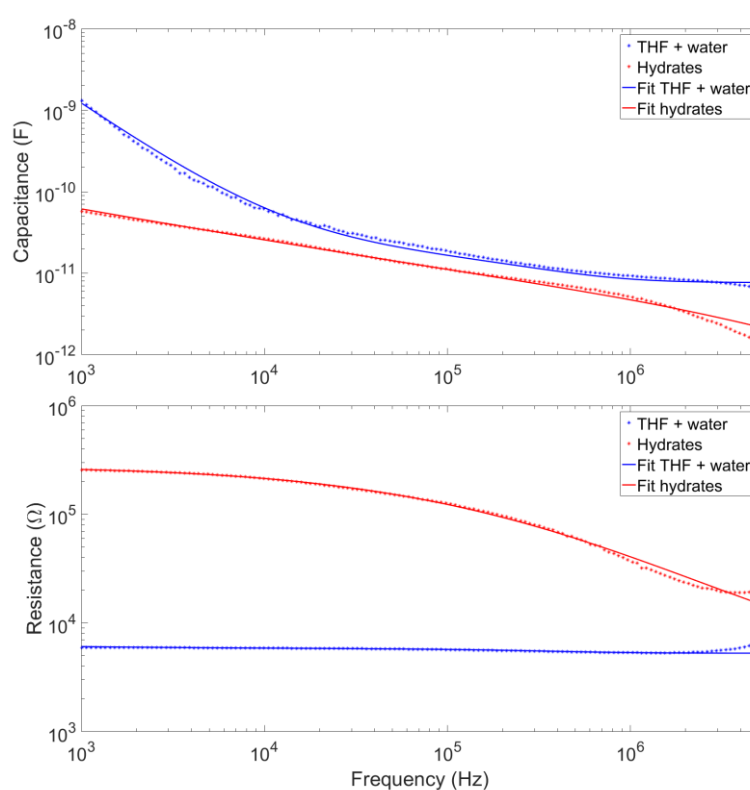
Source: Personal collection.

Likewise, the resistance response has similar behavior to that observed for ice, with the difference that here we do not have a relaxation process after the physical state change to the frequency of up to 5 MHz. So after solidification there are no abrupt

changes in resistance values, they only tend to stabilize. Such variation, as for ice, is due to the molecular arrangement that is different for the substance in liquid or solid state, which is detectable by EIS.

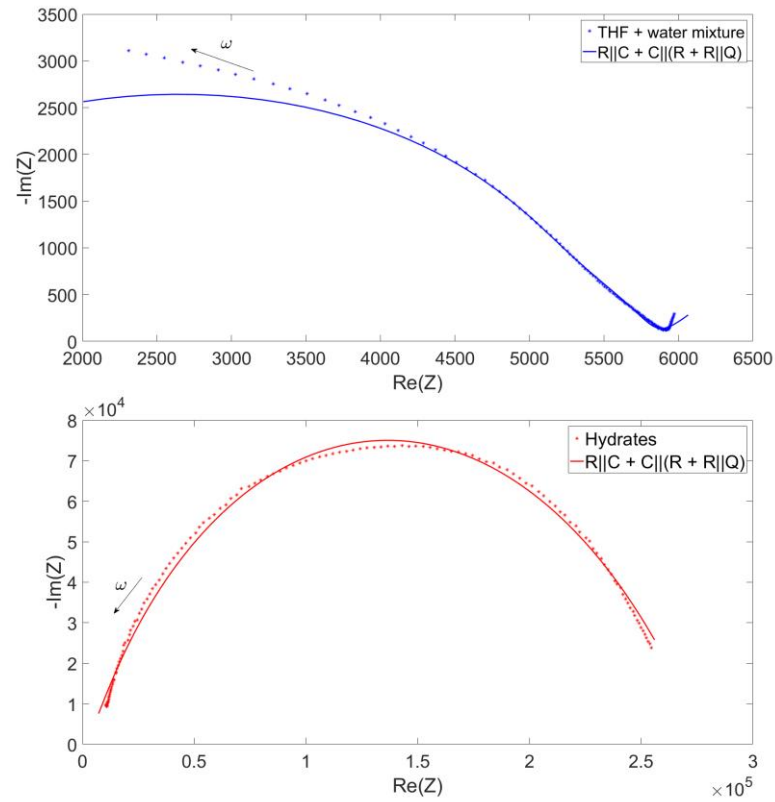
Applying the model, restricting the frequency range from 1 kHz to 5 MHz, we can see a good agreement between the measured data and the fit for capacitance and resistance (Figure 53).

Figure 53 - Capacitance and resistance bode plots for hydrates formation fitted with $R||C+C||(R+R||Q)$.



Source: Personal collection.

Converting to impedance for the THF + water mixture and hydrates (Figure 54) we can confirm that the proposed equivalent circuit is able to fit the liquid and solid analyte, being it water, THF + water mixture, ice or hydrates.

Figure 54 - THF + water mixture and hydrates impedance fitted with $R||C + C||(R + R||Q)$ using the combined sensor.

Source: Personal collection.

The parameters can be found in Table 7:

Table 7 - Parameters obtained from fitting impedance data for THF + water mixture and hydrates for the combined sensor.

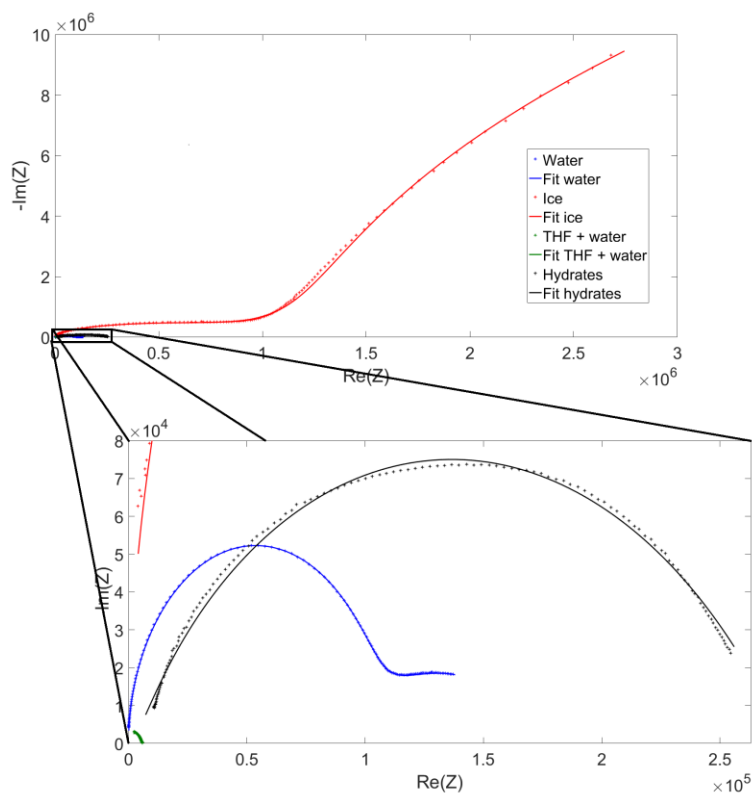
Parameters	THF + Water	Hydrates
R_1 (Ω)	5.16e03	5.10e06
τ_1 (s)	4.00e-08	3.57
R_2 (Ω)	7.54e02	1.15e04
τ_2 (s)	4.34e-07	2.23e-14
R_3 (Ω)	7.41e04	2.66e05
τ_3 (s)	1.37	5.46e-06
n_3	0.60	0.60
τ_4 (s)	1.64e-03	8.00e-07

Source: Personal collection.

For this experiment, during the liquid stage (THF + water mixture) the dominant circular arc is modeled by the $R||C$ circuit and the modified Randles circuit represents the small tail at low frequencies. For the solid stage (hydrates) the $R||C$ element is not even visible any longer as it is too small now and actually not necessary for the fit, the impedance in the whole frequency range is represented by the modified Randles circuit.

To get a better view of the results and compare them more easily, we can plot together the measured data and the fits for water, ice, THF + water mixture and hydrates in the same graph (Figure 55).

Figure 55 - Impedance plots for water, ice, THF + water mixture, hydrates and the fits plotted together.



Source: Personal collection.

Now it is easier to observe the differences in impedance spectra for all four substances and it is noticed that the ice and hydrates spectra are very discordant between each other, thus enabling the distinction using the applied model. This differentiation is more evident when we compare the fitted parameters from Table 4

with Table 6 and Table 5 with Table 7, especially when we counteract the τ times, showing the different relaxation times for each physical state or substance.

4.6 Applying the Relative Mean Absolute Error

Applying then the already explained MAE% (section 2.1.6), we have the following results (Table 8).

Table 8 - Calculated relative mean absolute error between data and fits

MAE (%)	Combined sensor	Commercial sensor
Water	1.25	0.15
Ice	2.51	2.41
THF+water	1.59	0.16
Hydrates	4.46	7.71

Source: Personal collection.

In most cases the error is less than 5%, which is satisfactory, i.e. the proposed fits, reflect the measured data. The commercial sensor is more well prepared to measure liquid samples, as the name suggests (Liquid dielectric test fixture – Section 3), so this is expected to have better fits from these data, what is confirmed for the low MAE% values. However, the combined sensor also shows satisfactory fits indicated by low MAE% values. It can be seen that MAE% values are lower for liquids (water, THF+water) and slightly higher values for solids (ice and hydrates). Thus, it indicates that the model chosen is better suited for the liquids, but satisfactory appropriate for solids. Also, another factor is that a single model is certainly not ideal for all cases. In future different equivalent circuit could be used for each case.

As the objective of the work is to be able to distinguish especially the hydrates spectra from the other substances, thus being able to detect the formation of such crystals, we can say that such percentage errors are acceptable and make the technique feasible.

4.7 Deadleg sensor experiments

Some validation experiments were performed to get used to the equipment and some software issues have been remedied. Then, using an appropriated vessel for ice formation known as glass jacketed beaker (250 ml) shown in

Figure 56, some ice experiments were performed. It was not possible to perform hydrates formation using THF because the PVC used in the sensor can be corroded by this chemical, so the hydrates formation should be performed only in the deadleg using gas.

Figure 56 - Glass jacketed beaker.



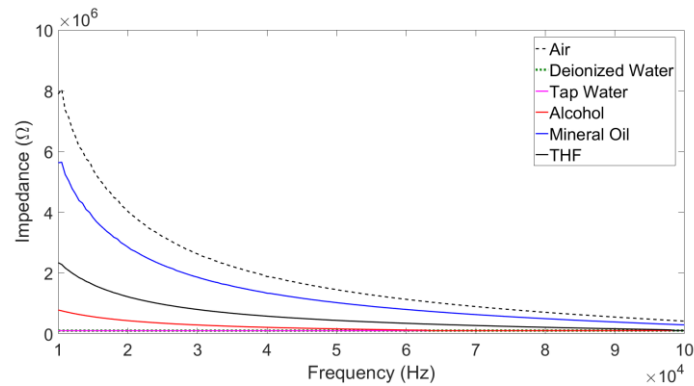
Source: Personal collection.

4.7.1 Verification experiments

Having already highlighted the reality about the use of deadlegs in the oil and gas industry (section 2.2.3) and in order to monitor the formation of hydrates in this scenario, the used electronics must be as simple and robust as possible. Bearing this in mind, the use of the impedance analyzer becomes unfeasible in the field, so we decided to do exploratory experiments using the cited evaluation boards (section 3.3.2). The AD5933 was chosen due to the possibility of generating an impedance spectrum as in the Keysight analyzer. The FDC2214 was chosen because it is resistant to external interference, has high resolution in the capacitance measurements and great industrial potential.

Using six standard substances the deadleg sensor was tested with the AD5933 (Figure 57) and FDC2214 (Figure 58).

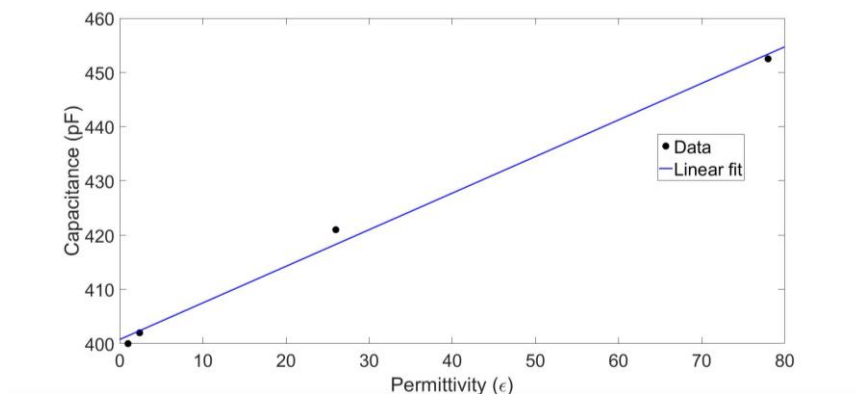
Figure 57 - Impedance spectra for standard substances using the AD5933 and deadleg sensor.



Source: Personal collection.

At CSM the deionized water is provided by a system that has a central and the liquid is sent to the whole building by specific pipes. In this way there was no specific control of each laboratory regarding the water quality and in the conductivity measurements the values were not as expected, being around $510 \mu\text{S}/\text{cm}$, which was high and also pretty close to the tap water value, making the impedance spectra of these two substances very similar.

Figure 58 – Linear behavior of the electronics regarding the measured capacitance and the permittivity values from literature for air, oil, alcohol and water.



Source: Personal collection.

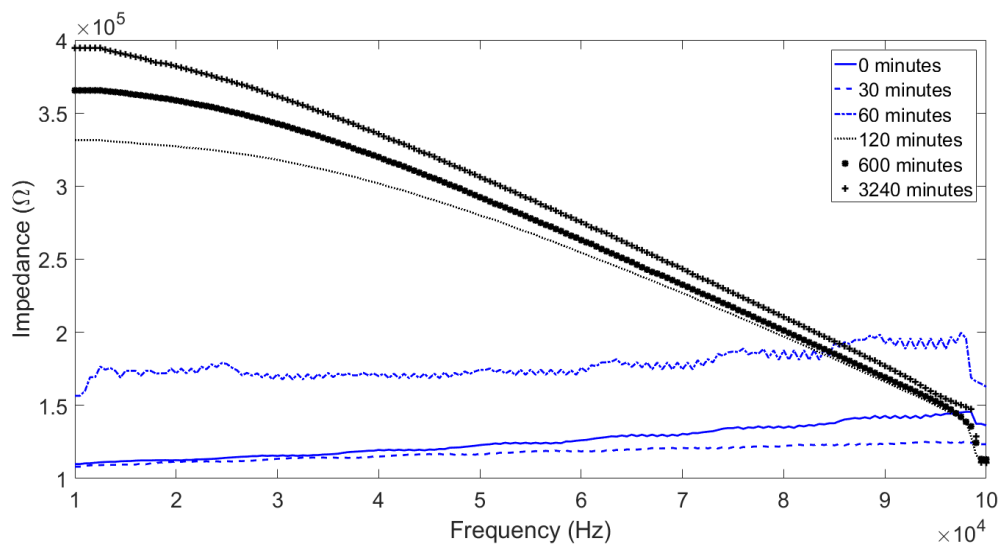
At this time the THF was not used because of the sensor corrosion but the main goal was to check the sensitivity of the sensor and electronics to different substances. For the FDC2214 the absolute values of capacitance may seem very close to each other,

but the high resolution of the electronics allows a precise detection of which substance is under analysis.

4.7.2 Ice formation monitoring

Setting the chiller temperature to $-5\text{ }^{\circ}\text{C}$ and with a room temperature of $20\text{ }^{\circ}\text{C}$, the deionized water inside the glass jacketed beaker started to cool down. The impedance spectra from AD5933 (Figure 59) and the capacitance values from FDC2214 (Figure 60) were monitored but in different experiments.

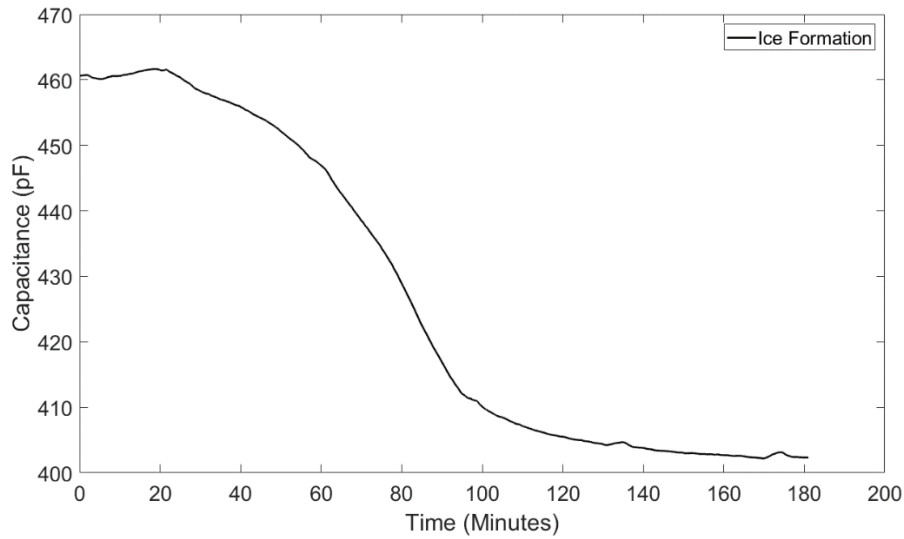
Figure 59 - Impedance spectra for ice formation using AD5933 and deadleg sensor.



Source: Personal collection.

The raw signal contains a significant amount of noise especially when the water is still in the liquid state because there are no shielding electrodes in this sensor geometry and the water is more conductive than ice, so for this case we used a median filter. We can see that as the temperature decreases the impedance also tends to decrease. However, when the H_2O molecules begin to expand due to anomalous behavior of water below $4\text{ }^{\circ}\text{C}$ and then ice crystals begin to form, we notice that impedance values start to increase specially for lower frequencies and the spectra as a whole change.

Figure 60 - Capacitance values for ice formation using FDC2214 and deadleg sensor.



Source: Personal collection.

Using the FDC electronics the capacitance values seems to stabilize as early as 180 minutes. Here it is also possible to observe an initial increase in capacitance values up to approximately 20 minutes and then the decay. Using the FDC2214 the phenomena seems to be detected earlier than using the AD5933, however this comparison may not be fair, since the experiments are not the same (although all conditions of pressure, temperature and water volume have remained the same), the nucleation time is not necessarily always the same in time. However, despite the small discrepancies in the onset time of each phenomenon that encompasses the solidification of water (already described in section 2.2.2) between one electronics and another, both systems were able to detect the change in physical state. These results are in agreement with the already observed in sections 4.2 and 4.3.2.

Having measured the ice formation with both electronics it seems that the one from Texas Instruments (FDC2214) is sufficient to detect the change of physical state inside the deadlegs. In other words, thinking only about detecting changes in physical state, there is no need of more complex and elaborated electronics (with the possibility of measuring spectrum).

5. Conclusion

In this final and concluding chapter, the main achievements of the thesis are summarized as well as some issues for future work are discussed.

5.1 Conclusions

A novel sensor is proposed using impedance spectroscopy as principle and allied to an optical sensor (FBG) for temperature measurements. The prototype sensor was housed in a composite material for ice and hydrates formation monitoring. It shows itself capable to measure changes in fluids, including its physical state change, as demonstrated using deionized water and the mixture with THF. As known, the ice and hydrates formation are a problem for industry and using techniques as presented in this work it is possible to monitor these formations and take appropriate preventive actions, once each substance has his own signature in impedance spectrum. The presented results are promising and show the potential of the system to be applied in industry in order to monitoring industrial process involving fluids.

The combination of two techniques in a single sensor allows to extract more information and to investigate more deeply some phenomena. The behavior of electrical impedance at the moment of water nucleation is a significant result and opens the way to more specific studies in this field.

Similarly, the problem of hydrate formation begins to be studied more deeply with the previous detection mentioned in this work. Combining the detection methods with the appropriate methodology for each phenomenon to be investigated and the correct processing of the monitored signals, the proposed technique has great potential and applicability to detect solids problems in pipes in the oil industry.

The main achievements are the understanding of impedance spectra of ice and hydrates, the possibility to distinguish and detect the solid formations and the proposal, application and validation of the generic model for data fitting. In this way, the proposed model can be used to differentiate the analyzed substances in this thesis, the

parameterization of the variables shows great potential for indicating a change in physical state and the systematic process for carrying out the experiments has been validated.

With the data presented in this thesis, we recommend the use of spectroscopy method in order to get the hole spectra so we can get more information about the phenomena, extract the parameters and have an overall idea of the possible relaxation process. In our case, to measure the hydrates formation it is possible to perform the frequency sweep since the time to take the measurement was not a determining factor. However, in other applications like flow patterns measurements, the measurement speed is a concern as phenomena is transient. Then, in order to measure faster phenomena or to reduce the costs it is more pertinent to choose a fixed frequency using a simpler electronics. Moreover, for field applications, the issue of ease of installation and operation can also be a determining factor in some cases, and the use of dedicated and simpler electronics can be more suitable as well.

5.2 Future development

Some activities can be listed as future works. The main points are:

- test in a pressurized cell with fluids more similar to the application, for instance use of oil and methane at pressure of few hundred bar;
- use of more FBG sensors. The current sensor geometry can be maintained and the use of the FBG sensor can be improved by inserting more than one sensing unit in different positions. The implication of the positioning of one more FBG in the impedance measurement region should be studied, but the FBG sensor and the material used to encapsulate it are non-electric conductors, thus having an advantage in this case when compared to thermocouples;
- construction and use of dedicated electronics for sweep frequency measurements;
- the use of another equivalent electric circuit model, trying to mimic better the data behavior and a more generalist approach for different kinds of substances;
- application of the developed sensor and data processing for flow loop measurements;
- increase sensor robustness for high-pressure and long-term applications

References

AGILENT. **Operation Manual**. Agilent 4294A Precision Impedance Analyzer, Agilent Technologies, 2003.

AGILENT. **Technical Overview**. Agilent 4294A Precision Impedance Analyzer 40 Hz to 110 MHz, 2008.

AKYURT, M.; ZAKI, G.; HABEEBULLAH, B. Freezing phenomena in ice-water systems. **Energy Conversion and Management**, v. 43, p. 1773-1789, 2002.

ALAVI, S. M. M.; BIRKL C. R.; BIRKL, D. A. Time-domain fitting of battery electrochemical impedance models. **Journal of Power Sources**, v. 288, p. 345-352, 2015.

ALOCILJA, E. C.; RADKE, S. M. Market analysis of biosensors for food safety. **Biosensors and Bioelectronics**, 18, 841-846, 2003.

Anon. **Theoretical aspects of the freezing process**, University of Guelph, 2000.

AOKI, K. J. Frequency-dependence of electric double layer capacitance without Faradaic reactions. **Journal of Electroanalytical Chemistry**, v. 779, p. 117-125, 2016.

ARULEPP, M.; PERMANN, L.; LEIS, J.; PERKSON, A.; RUMMA, K.; JANES, A.; LUST, E. Influence of the Solvent Properties on the Characteristics of a Double Layer Capacitor. **Journal of Power Sources**, v. 133, N .2, p. 320-328, 2004.

BANNWARTH, S.; DARESTANI, M.; COSTER H.; WESSLING, M.; Characterization of hollow fiber membranes by impedance spectroscopy. **Journal of Membrane Science**, v. 473, p. 318-326, 2015.

BARRER, R. M.; RUZICKA, D. J. Non-stoichiometric clathrate compounds of water. Part 4.—Kinetics of formation of clathrate phases. **Transactions of the Faraday Society**, v. 58, p. 2262-2271, 1962.

BARSOUKOV, E.; MACDONALD, J. R. **Impedance Spectroscopy: Theory, Experiment, and Applications**, Eds., Wiley-Interscience, 2005.

BERNAL, J. D.; FOWLER, R. H. A theory of water and ionic solution, with particular reference to hydrogen and hydroxyl ions. **The Journal of Chemical Physics**, v. 1, n. 8, p. 515-548, 1933.

BEVINGTON, P. R.; ROBINSON, D. K. **Data reduction and error analysis for the physical sciences**. 3rd edition, McGraw-Hill, New York NY. 2003.

BUCKLEY, F. and MARYOTT, A. A. **Tables of Dielectric Dispersion Data for Pure Liquids and Dilute Solutions**. U.S. Dept. of Commerce, National Bureau of Standards, USA. Circular 589, 1958.

CADY, P. Progress in impedance measurements in microbiology. Springfield: **Chapter 14 in "Mechanizing microbiology"** edited by Anthony N. Sharpe & David S. Clark, Charles C. Thomas Publisher., 199–239, 1978.

CECCIO, S. L.; GEORGE, D. L. A review of electrical impedance techniques for the measurement of multiphase flows. **Journal Fluids Engineering**, 118 391-399, 1996.

CHANSON, H. Air-Water Flow Measurements with Intrusive, Phase-Detection Probes: Can We Improve Their Interpretation? **Journal of Hydraulic Engineering**, v. 128, p. 252-255, 2002.

CHEN, S.-M.; RAMACHANDRAN, R.; MANI, V.; SARASWATHI, R. Recent advancements in electrode materials for the high-performance electrochemical supercapacitors: A review. **International Journal of Electrochemical Science**, 9 (8), p. 4072-4085, 2014.

CHEN, Z; HOJO, M. Relationship between triple ion formation constants and the salt concentration of the minimum in the conductometric curves in low-permittivity solvents. **The Journal of Physical Chemistry B**, v. 101, n. 50, p. 10896-10902, 1997.

CLAUSSEN, W. F. A Second Water Structure for Inert Gas Hydrates. **Journal of Chemical Physics**, v. 19, p. 1425, 1951a.

CLAUSSEN, W. F. Suggested Structures of Water in Inert Gas Hydrates. **Journal of Chemical Physics**, v. 19, p. 662, 1951b.

COLLETT, T. S.; DALLIMORE S. R. Detailed analysis of gas hydrate induced drilling and production hazards. **Proceedings of international conference on gas hydrates 4**, Yokohama, p. 47–52, 2002.

COLLIE, C. H.; HASTED, J. B.; RITSON, D. M. 1948. The dielectric properties of water and heavy water. **Proceedings of the Physical Society**, 60(2), p.145, 1948.

CRAIG, B. D. Corrosion in oil/water systems. **Materials performance**, v. 35, n. 8, 1996.

CSIKÓS, R.; FREUND, M.; KESZTHELYI, S.; MÓZES, G. Y. **Paraffin products, properties, technologies and applications**. Budapeste, Hungria: Elsevier, 1982.

DA SILVA, M. J. **Impedance Sensors for Fast Multiphase Flow Measurement and Imaging**. 2008. 170p. Tese (Doutorado) - Dresden: Fakultät Elektrotechnik und Informationstechnik, Technische Universität Dresden, 2008.

DA SILVA, M. J.; SCHLEICHER, E.; HAMPEL, U. Capacitance wire-mesh sensor for fast measurement of phase fraction distributions, **Measurement Science and Technology**, vol. 18, no. 7. pp. 2245–2251, 2007.

DAMSKIN, B.B.; PETRII, O.A. Historical Development of Theories of the Electrochemical Double Layer. **Journal of Solid State Electrochemistry**, v. 15, n. 7-8, p. 1317-1334, 2011.

DIAS, F. A., **Increasing Image Resolution for Wire-Mesh Sensor Based on Statical Reconstruction**. 68 p. Master Thesis – Graduate Program in Electrical and Computer Engineering (CPGEI), Federal University of Technology – Paraná (UTFPR). Curitiba, 2017.

DOS SANTOS, E. N., **Development and application of wire-mesh sensors for high-speed multiphase flow imaging**. 205 p. Doctoral Thesis – Graduate Program in Electrical and Computer Engineering (CPGEI), Federal University of Technology – Paraná (UTFPR). Curitiba, 2015.

DURANTE, G.; BECARI, W.; LIMA, F. A. S.; PERES, H. E. M. Electrical Impedance Sensor for Real-Time Detection of Bovine Milk Adulteration. **IEEE Sensors Journal**, 16 4, 861-865, 2016.

EISENBERG, D.; KAUZMANN, W. **The Structure and Properties of Water**, Oxford University Press, Oxford, 1969.

ELKOW, K. J.; REZKALLAH, K. S. Void fraction measurements in gas-liquid flows using capacitance sensors. **Measurement Science and Technology**, v. 7, n. 8, p. 1153-1163, 1996.

FALCONE, G.; HEWITT, G. F.; ALIMONTI, C. Multiphase Flow Metering: Principles and Applications – Developments in Petroleum Science. **Elsevier Science**, 2009.

FARADAY, M. On hydrate of chlorine. **Quarterly Journal of Science**, v. 15, p. 71-75, 1823.

FERNÁNDEZ-SÁNCHEZ, C.; MCNEIL, C. J., RAWSON, K.; Electrochemical impedance spectroscopy studies of polymer degradation: application to biosensor development. **Trends in Analytical Chemistry**, v. 24, p. 37-48, 2005.

FLETCHER, N. H. **The Chemical Physics of Ice**, Cambridge University Press, Cambridge, 1970.

FLOCKHART, G. M.; MAIER, R. R.; BARTON, J. S.; MACPHERSON, W. N.; JONES, J. D.; CHISHOLM, K. E; ZHANG, L., BENNION, I., READ, I., FOOTE, P. D. Quadratic behavior of fiber Bragg grating temperature coefficients. **Applied optics**, v. 43, n. 13, p. 2744-2751, 2004.

FOLGERØ, K. Broad-band dielectric spectroscopy of low-permittivity fluids using one measurement cell. In: **IEEE Transactions on Instrumentation and Measurement**, v. 47, p. 881-885, 1998.

GIACCHINI, B. L. **Uma breve introdução ao Método dos Elementos Finitos**. Departamento de Matemática, Instituto de Ciências Exatas, Universidade Federal de Minas Gerais, 2012.

GOUGH, S. R. The Structure of Ice Grown in Bulk Supercooled Water. **Canadian Journal of Chemistry**. 50, 3046 (1972).

GREGORY, A. P.; CLARKE, R. N. A review of RF and microwave techniques for dielectric measurements on polar liquids. **IEEE Transactions on Dielectrics and Electrical Insulation**, v. 13, n. 4, p. 727-743, 2006.

GREGORY, G. A.; MATTAR, L. An In-Situ Volume Fraction Sensor for Two-Phase Flows of Non-Electrolytes. **The Journal of Canadian Petroleum Technology**, v. 12, n. 2, 1973.

GROSSI, M.; RICCÒ, B. An automatic titration system for oil concentration measurement in metalworking fluids. **Measurement**, 97, 8-14, 2017.

GUO, B.; SONG, S.; GHALAMBOR, A.; LIN, T. R. **Offshore Pipelines. Design, Installation, and Maintenance**. 2nd Edition, GPP Elsevier, MA, 2014.

HABIB, M. A.; BADR, H. M.; SAID, S. A. M.; HUSSAINI, I.; AL-BAGAWI, J. J. On the development of deadleg criterion. **Journal of fluids engineering**, v. 127, n. 1, p. 124-135, 2005a.

HABIB, M. A.; BADR, H. M.; SAID, S. A. M.; MOKHEIMER, E. M. A.; HUSSAINI, I.; AL-SANAA, M. Characteristics of flow field and water concentration in a horizontal deadleg. **Heat and mass transfer**, v. 41, n. 4, p. 315-326, 2005b.

HAMMERSCHMIDT, E. G. Formation of gas hydrates in natural gas transmission lines. In: **Industrial and Engineering Chemistry**, v. 26, p. 851-855, 1934.

HARKER, F. R.; MAINDONALD, J. H. Ripening of nectarine fruit. **Plant Physiology**, 106, 165-171, 1994.

HAYNES, W. M. (ed). **CRC Handbook of Chemistry and Physics**, 96th ed. Boca Raton, FL: **CRC Press**, 2016.

HELGERUD, M. B.; WAITE, W. F.; KIRBY, S. H.; NUR, A. Elastic wave speeds and moduli in polycrystalline ice Ih, sI methane hydrate, and sII methane-ethane hydrate. **Journal of Geophysical Research**, 114, 2009.

HELMHOLTZ, H. v. Gesetze der Verteilung elektr. Ströme in körperlichen Leitern mit Anwendung auf tierische elektr. Versuche. **Annalen der physik**. Bd, v. 89, p. 211-233, 1853.

HILL, K. O.; MELTZ, G. Fiber Bragg grating technology fundamentals and overview, **Journal of Lightwave Technology**, Volume 15, no. 8, pp. 1263–1276, 1997.

HOU, Y. **Controlling variables of electric double-layer capacitance**. 108 p. Doctoral Thesis - Materials Engineering, Graduate School of University of Fukui. Japan, 2014.

ISMAIL, B.; AHMED, W. Innovative Techniques for Two-Phase Flow Measurements. **Recent Patents on Electrical Engineering**, v. 1, n. 1, p. 1-13, 2008.

JHA, S. N.; NARSAIAH, K.; BASEDIYA, A. L.; SHARMA, R.; Jaiswal, P.; Kumar, R.; BHARDWAJ, R. Measurement techniques and application of electrical properties for nondestructive quality evaluation of foods—a review. **Journal of food science and technology**, v. 48, n. 4, p. 387-411, 2011.

JOHNSON, M. L.; FRASIER, S. G. Nonlinear least-squares analysis. In: **Methods in enzymology**. Academic Press, p. 301-342, 1985.

KARAMODDIN, M.; VARAMINIAN, F. Performance of hydrate inhibitors in tetrahydrofuran hydrate formation by using measurement of electrical conductivity. **Journal of Industrial and Engineering Chemistry**, v. 20, p. 3815–3820, 2014.

KASHCHIEV, D.; FIROOZABADI, A. Driving force for crystallization of gas hydrates. **Journal of Crystal Growth**, v. 241, 220-230, 2002a.

KASHCHIEV, D.; FIROOZABADI, A. Nucleation of gas hydrates. **Journal of Crystal Growth**, v. 243, p. 476-489, 2002b.

KERSEY, A. D.; DAVIS, M. A.; PATRICK, H. J.; LEBLANC, M.; KOO, K. P.; ASKINS, C. G.; PUTNAM, M. A.; FRIEBELE, E. J. Fiber Grating Sensors. **Journal of Lightwave Technology**, 15 (1997), p. 1442

KEYSIGHT. **16048A Test Leads**. Operation and Service Manual, Keysight Technologies, 2016a.

KEYSIGHT. **16452A Liquid Test Fixture**. Operation and Service Manual, Keysight Technologies, 2017.

KEYSIGHT. **Basics Of Measuring The Dielectric Properties Of Material**, USA. Application Note, 2019.

KEYSIGHT. **Impedance Measurement Handbook**. 6th Edition. Application Note, Keysight Technologies, 2016b.

KIM, C. H.; PYUN, S. I.; KIM, J. H. Kim. An Investigation of the Capacitance Dispersion on the Fractal Carbon Electrode with Edge and Basal Orientations. **Electrochimica Acta**, v. 48, N. 23, p. 3455-3463, 2003.

KINNARI, K. J.; M. ASKVIK, K.; LI, X.; AUSTVIK, T.; ZHANK, X.; SA, J. H.; SUM, A. K. Hydrate Management of Deadlegs in Oil and Gas Production Systems—Background and Development of Experimental Systems. **Energy & Fuels**, v. 31, n. 11, p. 11783-11792, 2017.

KOH, C. A.; SUM, A. K.; SLOAN, E. D. State of the art: Natural gas hydrates as a natural resource. **Journal of Natural Gas Science and Engineering**, v. 8, p. 132-138, 2012.

KOPP, M. Conductivité électrique de la neige, au courant continu. **Zeitschrift für angewandte Mathematik und Physik**, Bd. 13, Ht. 5, p. 431 – 441, 1962.

KOZA, M.; SCHOBER, H.; TÖLLE, A.; FUJARA, F.; HANSEN, T. Formation of ice XII at different conditions. **Nature**, 397, 660-661, 1999.

KUMBHARKHANE, A. C.; HELAMBE, S. N.; LOKHANDE, M. P.; DORAISWAMY, S.; MEHROTRA, S. C. Structural study of aqueous solutions of tetrahydrofuran and acetone mixtures using dielectric relaxation technique. **PRAMANA Journal of Physics**, v. 46, n. 2, 1996.

KURIG, H.; VESTLI, M.; JANES, A.; LUST, E. Electrical Double Layer Capacitors Based on Two 1-Ethyl-3-Methylimidazolium Ionic Liquids with Different Anions. **Electrochemical and Solid-State Letters**, v.14, n .8, p. A120-A122, 2011.

LEITZKE, J. P. **Development of a fluids monitoring system based on impedance spectroscopy**. 71 f. Monografia (Mestrado em Engenharia Elétrica) – Programa de Pós-Graduação em Engenharia Elétrica e Informática Industrial, Universidade Tecnológica Federal do Paraná. Curitiba, 2014.

LERVIK, J. K.; KULBOTTEN, H.; KLEVJER, G. Prevention of hydrate formation in pipelines by electrical methods. In: **Proceedings of the Seventh International Offshore and Polar Engineering Conference**. p. 25-30, 1997.

LOBBAN, C.; FINNEY, J. L.; KUHS, W. F. The structure of a new phase of ice. **Nature**, v. 391, n. 6664, p. 268-270, 1998.

LONGO, J. P. N. **Electrical Impedance Measurements of Clathrate Hydrates**. 84 p. Master Thesis (Graduate Program in Electrical and Computer Engineering of Federal University of Technology – Paraná.). Curitiba, 2015.

LONGO, J. P. N.; LEITZKE, J. P.; MORALES, R. E.; DA SILVA, M. J. Simple measuring system for impedance spectroscopy analysis of fluids. **Instrumentation Systems, Circuits and Transducers (INSCIT)**, International Symposium on (pp. 77-80). IEEE, 2016.

LONGO, J. P.; WRASSE, A.; SANTOS, E.; SILVA, M.; MORALES, R. E. Sensor capacitivo interdigital para detecção de deposição de parafina em oleodutos. In: **Congresso Brasileiro de Automática**, 2014.

LUDWIG, R. Water: From Clusters to the Bulk. **Angewandte Chemie International Edition**, 40: 1808–1827, 2001.

MACDONALD, J. R. Impedance Spectroscopy. In **Annals of Biomedical Engineering**, v. 20, p. 289-305, 1992.

MACDONALD, J. R. **Impedance Spectroscopy**. New York: John Wiley & Sons. 1987.

MACKINTOSH, N.; ATAKAN, Z. Flow assurance still leading concern among producers. **Offshore** (Conroe, Tex.), v. 60, n. 10, p. 79-174, 2000.

MACKLIN, W. C.; RYAN, B. F. The structure of ice grown in bulk supercooled water. **Journal of the Atmospheric Sciences**, v. 22, n. 4, p. 452-459, 1965.

MAK, C. W.; MCMULLAN, R. K. **Journal of Chemical Physics**, v. 42, p. 2732, 1965.

MCMULLAN, R. K.; JEFFREY, G. A. Polyhedral Clathrate Hydrates. IX. Structure of Ethylene Oxide Hydrate. In: **Journal of Chemical Physics**, v. 42, p. 2725, 1965.

MIALICH, M. S.; FACCIOLI SICCHIERI, J. M.; ALCEU, A. J. J. Analysis of Body Composition: A Critical Review of the Use of Bioelectrical Impedance Analysis. **International Journal of Clinical Nutrition**, 2 1, 1-10, 2014.

MIHAJLOVIĆ, V.; GRUNDLEHNER, B.; VULLERS, R.; PENDERS, J. Wearable, wireless eeg solutions in daily life applications: What are we missing? **IEEE Journal of Biomedical and Health Informatics**, v. 19, n. 1, p. 6–21, 2015.

MORITA, M.; GOTO, M.; MATSUDA, Y.. Ethylene Carbonate-Based Organic Electrolytes for Electric Double Layer Capacitors. **Journal of Applied Electrochemistry**, v. 22, n.10, p. 901-908, 1992.

MORRIS, B.; DAVIDSON, D. W. A Clathrate Hydrate of Cyclobutanone: Dielectric Relaxation of the Host and Guest Molecules. **Canadian Journal of Chemistry**, v. 49, n. 8, p. 1243-1251, 1971.

MOTULSKY, H. J.; CHRISTOPOULOS, A. **Fitting models to biological data using linear and nonlinear regression. A practical guide to curve fitting**. GraphPad Software Inc., San Diego CA. 2003.

MULLIN, J. W. **Crystallization**, 3rd Edition, Butterworth-Heinmann, Oxford, U.K, 1993.

OTHONOS, A. Fiber bragg gratings, **Review of Scientific Instruments**, vol. 68, no. 12, pp. 4309–4341, 1997.

PAULING, L.; MARSH, R. E. The structure of chlorine hydrate. **Proceedings of the National Academy of Sciences**, v. 38, n. 2, p. 112-118, 1952.

POWELL, H. M. The structure of molecular compounds. Part IV. Clathrate compounds. In: **Journal of the Chemical Society**, p. 61-73, 1948.

PRASSER, H.-M.; BÖTTGER, A.; ZSCHAU, J. A new electrode-mesh tomograph for gas-liquid flows, **Flow Measurement and Instrumentation**, vol. 9, no. 2, pp. 111–119, 1998.

RAHN, C. D.; WANG, C.-Y. Battery Systems Engineering. **Hoboken**, NJ, USA: Wiley, 2013.

RANDLES, J. E. B. Kinetics of rapid electrode reactions. **Discussions Faraday Society**, v. 1, p. 11–19, 1947.

RAO, Y. J. Recent progress in applications of in-fibre Bragg grating sensors. **Optics and Lasers Engineering**. V. 31, p. 297–324, 1999.

RIBEIRO, D. V.; ABRANTES, J. C. C. Application of electrochemical impedance spectroscopy (EIS) to monitor the corrosion of reinforced concrete: A new approach. **Construction and Building Materials**, v. 111, p. 98-104, 2016.

RODRIGUES, S.; MUNICHANDRAIAH, N.; SHUKLA, A. K. A review of state-of-charge indication of batteries by means of a.c. impedance measurements. **J. Power Sources**, 87, 12-20, 2000.

ROLDAN-CRUZ, C.; VERNON-CARTER, E. J.; ALVAREZ-RAMIREZ, J. Assessing the stability of Tween 80-based O/W emulsions with cyclic voltammetry and electrical impedance spectroscopy. **Colloids and Surfaces A: Physicochemical and Engineering Aspects**, 511, 145-152, 2016.

SA, J. H.; LEE, B. R.; ZHANG, X.; KINNARI, K. J.; LI, X.; ASKVIK, K. M.; SUM, A. K. Hydrate Management in Deadlegs: Hydrate Deposition Characterization in a 1-in. Vertical Pipe System. **Energy & Fuels**, v. 31, n. 12, p. 13536-13544, 2017.

SCHLÜTER, V. G. Entwicklung eines experimentell gestützten Bewertungsverfahrens zur Optimierung und Charakterisierung der Dehnungsübertragung oberflächenapplizierter Faser-Bragg-Gitter-Sensoren. **BAM**, 2010.

SCHULSON, E. M. The Structure and Mechanical Behavior of Ice - **Journal of the Minerals, Metals & Materials Society**, v. 51 (2), p. 21-27, 1999.

SEKINE, I. Recent evaluation of corrosion protective paint films by electrochemical methods. **Progress in Organic Coatings**, 31, 73-80, 1997.

SEO, Y.; LEE, H.; RYU, B. Hydration number and two-phase equilibria of CH₄ hydrate in the deep ocean sediments, In: **Geophysical Research Letters**, v. 29, p. 85, 2002.

SLOAN, E. D. **Clathrate Hydrates of Natural Gases**. 2nd Edition, Marcel Dekker, Inc., New York, NY, 1998.

SLOAN, E. D. Fundamental principles and applications of natural gas hydrates. **Nature**, v. 426, n. 6964, p. 353-359, 2003.

SLOAN, E. D. Introductory overview: Hydrate knowledge development. In: **American Mineralogist**, v. 89, p. 1155-1161, 2004.

SLOAN, E. D.; KOH, C. A. **Clathrate Hydrates of Natural Gases**, 3rd Edition, CRC Press, New York, 2008.

SLOAN, E. D.; KOH, C.; SUM, A. K. **Natural Gas Hydrates in Flow Assurance**, GPP Elsevier, MA, 2010.

STILLINGER, F. H. Water revisited. **Science**, v. 209, n. 4455, p. 451-457, 1980.

STOJEK, Z. The Electrical Double Layer and Its Structure. In: Scholz F. et al. (eds) **Electroanalytical Methods**. Springer, Berlin, Heidelberg, 2010.

STRAZZA, D.; DEMORI, M.; FERRARI, V.; POESIO, P. Capacitance sensor for hold-up measurement in high-viscous-oil/conductive-water core annular flows. **Flow Measurement and Instrumentation**, 2011.

SUM, A. K.; BURRUSS, E. C.; SLOAN, E. D. Measurement of clathrate hydrates via Raman spectroscopy. In: **Journal of Physical Chemistry B**, v. 101, p. 7371-7377, 1997.

SUM, A. K.; ZHANG, X.; SA, J.; LEE, B. R.; AUSTVIK, T.; LI, X.; ASKVIK, K. M. Hydrate Management for Hydrate Deposition in Gas-Filled Vertical Pipes. **Offshore Technology Conference**, 2019.

THORN, R.; JOHANSEN, G. A.; HJERTAKER, B. T. Three-phase flow measurement in the petroleum industry. **Measurement Science and Technology**, v. 21, n. 1, 2013.

TSE, J. S.; KLEIN, M. L.; MCDONALD, I. R. Molecular dynamics studies of ice Ic and the structure I clathrate hydrate of methane. **The Journal of Physical Chemistry**, 87 (21), p. 4190-4203, 1983.

VANGARI, M.; PRYOR T.; JIANG, L. **Journal of Energy Engineering**. 139, 72, 2013.

VENKATESH, M. S.; RAGHAVAN, G. S. V. An overview of dielectric properties measuring techniques. **Canadian biosystems engineering**, v. 47, n. 7, p. 15-30, 2005.

VON STACKELBERG, M. **Recueil des Travaux Chimiques des Pays-Bas Journal of the Royal Netherlands Chemical Society**, v. 75, p. 902, 1956.

VON STACKELBERG, M. Solid Gas Hydrates. In: **Die Naturwissenschaften**, v. 3612, p. 359-362, 1949.

VON STACKELBERG, M. **Zeitschrift Elektrochem.**, v. 58, p. 104, 1954.

VON STACKELBERG, M.; MÜLLER, H. R. **Die Naturwissenschaften**, v. 38, p. 456, 1951a.

VON STACKELBERG, M.; MÜLLER, H. R. On the structure of gas hydrates. **The Journal of Chemical Physics**, v. 19, n. 10, p. 1319-1320, 1951b.

WALLENBERGER, F. T.; BINGHAM, P. A. **Fiberglass and glass technology. Energy-Friendly Compositions and Applications**. Springer, New York, 2010.

WALTRICH, P. J.; FALCONE, G.; BARBOSA JR., J. R. Axial development of annular, churn and slug flows in a long vertical tube. In: **International Journal of Multiphase Flow**, v. 57 p. 38-48, 2013.

WEBSTER, J. G. **The Measurement, Instrumentation and Sensors Handbook**. CRC Press LLC, 1999.

WEE, F. H.; SOH, P. J.; SUHAIZAL, A. H. M.; NORNIKMAN, H.; EZANUDDIN, A. A. M. Free space measurement technique on dielectric properties of agricultural residues at microwave frequencies. In: 2009 SBMO/IEEE MTT-S **International Microwave and Optoelectronics Conference (IMOC)**. IEEE, p. 183-187, 2009.

WEITEMEYER, K.; CONSTABLE, S.; KEY, K. Marine EM techniques for gas-hydrate detection and hazard mitigation. **The Leading Edge**, v. 25, n. 5, p. 629-632, 2006.

WRASSE, A. N. **Capacitive Sensor for Direct Imaging of Two-Phase Flows**. 81 p. Dissertação – Programa de Pós-Graduação em Engenharia Elétrica e Informática Industrial, Universidade Tecnológica Federal do Paraná. Curitiba, 2015.

YE, J.; PENG, L.; WANG, W.; ZHOU, W. Helical Capacitance Sensor-Based Gas Fraction Measurements of Gas-Liquid Two-Phase Flow in Vertical Tube with Small Diameter. **IEEE Sensors Journal**, v. 11, n. 8, p. 1704-1710, 2011.

ZUO, Y.; PANG, R.; LI, W.; XIONG, J. P.; TANG, Y. M. The evaluation of coating performance by the variations of phase angles in middle and high frequency domains of EIS. **Corrosion Science**, 50, p. 3322-3328, 2008.

Appendix A

Experimental methodology manual

Measurement of impedance in liquid materials using the Impedance Analyzer 4294A and test accessory for liquids 16452A.

A.1 Preparation

The 4294A Impedance Analyzer needs 30 minutes of on-time power to stabilize its operation, only after that time the experiment can be started. The 16048A (Figure A 1) test cable (BNC connector and BNC connector plate) is used to connect the 16452A commercial cell to the impedance analyzer.

Figure A 1 - 16048A test cable.

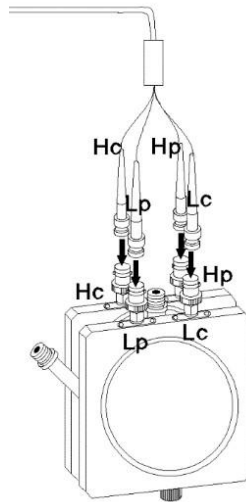


Source: Keysight (2016a).

The connector on the SMA cell is therefore necessary to connect the SMA to BNC adapters included in the access points 16452A (Figure A 2), to couple the test lead to the cell. It is always important to check the adapter's position during the experiments, as they may come loose, altering the results significantly. Each connector

on the cell has an identifier (Hcur, Lcur, Hpot, Lpot), which must match the identification on the test lead.

Figure A 2 - Cell 16452A.



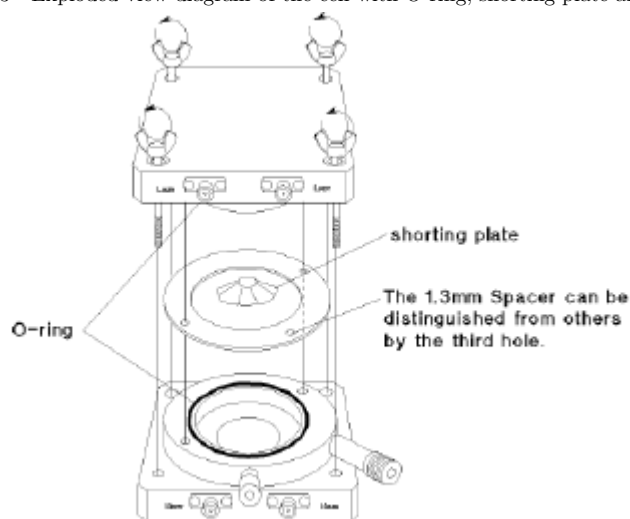
Source: Adapted from Keysight (2017).

A.2 Calibration

After the preparation step, the equipment must go through the calibration process. This is necessary because the test lead and the cell have imputed impedances due to the capacitance, inductance, and resistance inherent in these components, which must be disregarded in the measurements.

The procedure begins with the opening of the cell, which must be made by unscrewing four screws. These screws should be loose diagonally and carefully to avoid damaging the cell. As in the Figure A 3, the O-ring should be placed in its position, then the spacer 1.3 mm (distinguishable from the others by the presence of three holes, rather than two) and the short-circuit board/ring. The short circuit board/ring must be in contact with the two central electrodes. Then the cell is closed, threading diagonally and carefully, avoiding that the assembly is skewed. The bolts must be tightened so that the valve is tightly closed, as the instructions may change if this is not done.

Figure A 3 - Exploded view diagram of the cell with O-ring, shorting plate and spacer.



Source: Keysight (2017).

With the impedance analyzer switched on for more than 30 minutes the calibration process can be started, following the sequence of procedures:

- Set the initial and final scan frequencies to 40 Hz and 5 MHz, respectively.
 - To select the initial frequency as 40 Hz press the [Start] button of the block STIMULUS and then the [4], [0] and [x1] buttons of the ENTRY block.
 - To select the final frequency as 5 MHz press the [Stop] button of the block STIMULUS and then the [5] and [M / μ] buttons of the ENTRY block.
- Select the measurement for inductance and equivalent resistance series (Ls-Rs).
 - Press the MEASUREMENT block [Meas] button and select the item "Ls-Rs".
- Apply auto-scale.
 - Press the [A] button of the ACTIVE TRACE block to select the Ls marker.
 - Press the [Scale Ref] button of the MEASUREMENT block and select the AUTO SCALE item.

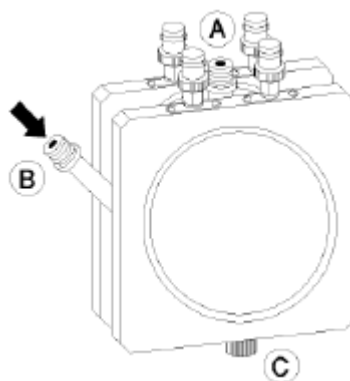
- Press the [B] button of the ACTIVE TRACE block to select the Rs marker.
- Press the [Scale Ref] button of the MEASUREMENT block and select the AUTO SCALE item.
- Set Marker to 1 MHz.
 - Press the [Marker] button of the MARKER block and then the [1] and [M / μ] buttons of the ENTRY block.
- Set the sweep to logarithmic scale.
 - Press the [Sweep] button of the STIMULUS block and select the TYPE item and then LOG.
- With the cell duly connected, the value at Ls must be ≤ 20 nH and $R_s \leq 0.5$ Ohm. If this does not happen the assembly and procedure should be re-evaluated.
- Select the measurement for parallel equivalent capacitance and resistance (Cp-Rp).
 - Press the MEASUREMENT block [Meas] button and then the "more 1/3", "more 2/3", "other" and "Cp-Rp" items.
- Perform short compensation.
 - Press the [Cal] button of the MEASUREMENT block and then the FIXTURE COMPEN and Short items.
- Remove the short circuit board/ring.
- Check the value, at the top of the screen, for Cp in the air. With the largest spacer the CP should be $5.5 \text{ pF} \pm 10\%$ or, using the smaller spacer (1.3 mm), $34.9 \text{ pF} \pm 25\%$. If this does not happen the assembly and procedure should be re-evaluated.

A.3 Experiment

Before starting the experiment make sure that the liquid outlet "C" (Figure A 4) is sealed (including O-ring) and that the tube "A" is open. In addition, if another liquid

has been analyzed previously the cell must be thoroughly sanitized using alcohol or any product that removes waste properly. The liquid is added through the tube "B", slowly in order to avoid bubbles formation until the cell is completely full (the liquid will appear on the edge of tube "A"). Acquisition can then be started.

Figure A 4 - Cell channels.



Source: Adapted from Keysight (2017).


Acquisitions are performed through a program made in Excel Visual Basic for Application (VBA). The connection of the PC to the impedance analyzer is made via a GPIB cable, and the address is 17 as a standard. When pressing the "Handshake" button an OK message should appear confirming the connection to the analyzer. To make the acquisition, you must select a name and press the "Get Data" button. The acquisition takes a few seconds and a new worksheet with the data is added to the file. A print screen of the program can be seen in Figure A 5.

Figure A 5 - Print screen of impedance analyzer program.

4294A Data Transfer Program

Rev.03.10

This program (Excel VBA) transfers the measurement data and the display image from the 4294A to a PC. Perform the single trigger measurement before running this program.
Enable 'Macros' first since this file contains macros
 For more details, refer to the operation manual



Step-1

Connect your PC with 4294A using either LAN cable or USB/GPIB interface. To handshake with 4294A, select the connection type and enter the GPIB address or the IP address of the 4294A, then click "Handshake" button.

GPIB

Connection Status

--	--

Step-2

Enter a new sheet name to transfer the measurement data or/and the display image, then click "Get Data" or/and "Get Image" button. The data/image is transferred to the newly created sheet.

Error Message

--

Source: Personal collection.

When an acquisition was made, try to synchronize the start of the acquisition with the on-screen scan of the impedance analyzer, so there will be no jumps in the data obtained (the acquisition is an exact copy of the data present on the analyzer screen at any given time).

It is interesting that, in addition to the acquisition file generated by the "4294A Data Transfer Program", a "Annotations.txt" file be created with a brief description of the experiment, the type of cell used, the date and, where relevant, the temperature the environment. In addition, for each acquisition, the marker value, previously defined to 1 MHz, must be entered for the capacitance and resistance at the moment they are performed, together with the name of the data generated by the acquisition.

The first acquisition is made with the cell still empty and clean, it must always be called c0 and will be used as a reference.